TWO FORMS OF SECONDARY HAWAIIAN VOLCANISM

A THESIS SUBMITTED TO THE GRADUATE DIVISION OF THE
UNIVERSITY OF HAWAI'I IN PARTIAL FULFILLMENT OF THE
REQUIREMENTS FOR THE DEGREE OF

MASTER OF SCIENCE

IN

GEOLOGY AND GEOPHYSICS

AUGUST 2004

By Todd Anthony Bianco

Thesis Committee

Garrett Ito, Chairperson
Janet Becker
Michael O. Garcia
Pål Wessel

We certify that we have read this thesis and that, in our opinion, it is satisfactory in scope and quality as a thesis for the degree of Master of Science in Geology and Geophysics.

THESIS COMMITTEE

_____

Chairperson

_____

_____

_____

Acknowledgements

Abstract

    This thesis addresses causes of two forms of secondary Hawaiian volcanism: rejuvenated onshore eruptions and offshore Hawaiian Arch flows. It is proposed that secondary volcanism is generated as a direct consequence of lithospheric flexural uplift that surrounds new volcanic shields as they grow. This uplift causes decompression of the underlying asthenosphere, which is assumed to be chemically and isotopically heterogeneous, near its solidus, and derived from the Hawaiian mantle plume. Uplift is modeled as the axisymmetric response of an elastic plate to a (volcanic) point load that grows linearly in time. To model flow in the asthenosphere, the rate of flexure of the lithosphere is taken as the upper boundary condition on an isoviscous, incompressible, fluid half-space. The first feature of secondary volcanism this model explains is the observed spatial gap between secondary volcanism and active shields. Best agreement is found with the majority of the observed spatial gaps with a lithosphere of effective elastic thickness T_e = 25-35 km. Secondly, this work demonstrates that the flexural model can produce observed crustal production if some magma focusing toward individual eruption sites occurs from the mantle over an area two to ten times the eruption area. The third feature this model addresses is that secondary lavas are isotopically distinct from shield lavas. In this model, melting the same two-component mantle forms the secondary and shield lavas, but the components are sampled by melting at rates that differ between the locations as predictable functions of depth. Flexural decompression produces melts that preferentially sample the mantle component that begins melting shallowest and which is associated with Sr and Nd isotope ratios most like those of secondary lavas. Melting in the center of a mantle plume is assumed to generate shield volcanism and is predicted to

preferentially sample the component that begins melting deepest which is associated with Sr and Nd isotope ratios more similar to shield lavas. Models therefore successfully predict the observed mean difference in $^{87}Sr/^{86}Sr$ and $^{143}Nd/^{144}Nd$ compositions between the secondary and shield lavas. The fourth feature addressed is that secondary lavas are alkalic and shield lavas are dominantly tholeiitic. To explain this difference, the mean extent of partial melting is computed, and it is found that a model plume composed mostly of depleted peridotite (90%) and some pyroxenite (10%) will yield a lower extent of melting for secondary lavas than shield lavas. This particular model assumes lithospheric thicknesses (90-100 km) and plume potential temperatures (mean of 1550 ^{o}C) that are consistent with independent studies of the Hawaiian hotspot. Thus, asthenospheric melting by flexural decompression is a viable mechanism of intraplate volcanism, which can explain many general characteristics of secondary Hawaiian volcanism.

Table of Contents

List of Tables

List of Figures

1. Introduction

The Hawaiian Islands, located on the center of the Pacific plate (Figure 1), are commonly believed to be formed by a mantle plume (*Wilson*, 1963). Four stages of eruptions have been described for Hawaiian volcanism (*Moore et al.*, 1982; *Clague and Dalrymple*, 1987). The growth begins with the alkalic preshield stage and continues with the tholeiitic main shield stage followed by the alkalic postshield volcanism. These shield stages are readily explained by melting of the plume, with the main shield stage occurring at the center of the plume. The final stage is the rejuvenation alkalic eruptions (or post-erosional lavas). At least five Hawaiian Islands have rejuvenation eruptions (Niihau, Kauai, Oahu, Molokai, and Maui), but the cause of this final stage is not well understood.

A defining characteristic of rejuvenation eruptions is that they follow a long period (>0.25 to 2.5 myr.) of volcanic quiescence. The time gap between shield and rejuvenation volcanism also results in a spatial gap since the Pacific plate is moving (~10 cm/yr) relative to the hotspot center, where the shields are built (*Clague and Dalrymple*, 1987). Figure 2 shows the current distance of volcanoes from the presumed location of the hotspot, beneath Kilauea (*Clague and Dalrymple*, 1987, 1988; *Tagami et al.*, 2002; *Ozawa et al.*, 2003). On this plot the reader should note that rejuvenation on one island occurs during the shield stage of another island. This plot also includes a fifth type of Hawaiian eruption, the North and South Arch Volcanic Fields (*Lipman et al.*, 1989; *Clague et al.*, 1990; *Dixon et al.*, 1997). The spacing and timing of these volcanic fields with respect to shield volcanoes suggests that they are an offshore version of rejuvenated volcanism (*Taylor et al*, 2004).

A second characteristic of rejuvenation lavas is that the eruptive volume flux is orders of magnitude smaller than at the shield (*Walker*, 1990). The North Arch lavas cover an expansive area (~2.5 x10^4 km^2), but are estimated to be only tens of meters thick on average (*Clague et al.*, 2002). This indicates that both on- and off-shore eruptions are relatively small compared to the shield stage volcanism which accounts for ~95-98% of a volcano's mass (*Clague and Dalrymple*, 1987).

Another characteristic of rejuvenation lavas is that they have higher ^{143}Nd/^{144}Nd and lower ^{87}Sr/^{86}Sr values than shield lavas (*Roden et al.*, 1984, *Clague and Dalrymple*, 1988; *Yang et al.*, 2003; Figure 3). Arch lavas are isotopically similar to the onshore rejuvenation lavas (*Clague et al.*, 1990; *Dixon et al.*, 1997; *Frey et al.*, 2000; *Yang et al.*, 2003). Hence, both arch and rejuvenation lavas are isotopically distinct from shield lavas.

Finally, a fourth characteristic of both the arch and rejuvenated lavas is that their major element compositions are alkalic, suggesting these develop from relatively low degrees of partial melting. This characteristic is distinct from the voluminous tholeiitic shield stage of volcanism. These tholeiitic lavas indicate higher degree of melting at the hotspot center (*Mysen and Kushiro*, 1977).

Above I have listed four similarities between rejuvenated and arch volcanism that distinguish them from shield volcanism. Following Stearns (1967) and Taylor *et al.* (submitted, 2004) this thesis will thus consider rejuvenation and arch volcanism as the same type of volcanism, and refer to them collectively as "secondary" volcanism. Correspondingly, I propose that the best model to explain secondary volcanism would

predict both onshore and offshore forms, as well as their differences from shield volcanism.

Three geophysical models have been proposed for onshore secondary volcanism. The most recent model, a dynamic plume model (*Ribe and Christensen*, 1999), has a second melting zone downstream from the hotspot. This second zone of melting is the result of asthenospheric upwelling and decompression as material expands beneath and interacts with the moving lithosphere. The melting region is confined to the base of the plume layer material and is approximately 320-520 km downstream from the center of the hotspot for the particular model parameters tested. This model successfully predicts a spatial gap between hotspot and rejuvenation eruptions. The model also predicts low extents of melting for rejuvenation lavas and higher extents of melting at the hotspot center. The weaknesses of this model are that it fails to predict arch volcanism and does not address the isotope compositions of the secondary volcanism.

In a second model, hot plume material rapidly reheats the lithosphere and resets lithospheric geotherms to resemble those of younger lithosphere (*Detrick and Crough*, 1978; *Crough*, 1978; *Guirret*, 1987; *Liu and Chase* 1991). During the process, the reheated lithosphere melts to supply rejuvenated volcanism. This model successfully explains the observed topographic high and gravity anomaly along the Hawaiian Chain. The model also predicts relatively small volumes of rejuvenation lavas compared to shield volcanism. Further, the model invokes melting of lithosphere to explain the isotope character of rejuvenation lavas, and the model predicts low extents of melting as prescribed for alkalic lavas. The weaknesses of this model are that it does not predict the

observed time gap preceding rejuvenation volcanism. This work also does not consider volcanism well away from the axis of the hotspot chain where arch volcanism occurs.

The third model attributes rejuvenated volcanism to lithospheric flexure (*Jackson and Wright*, 1970; *Clague and Dalrymple*, 1987; *ten Brink and Brocher*, 1987). The growing load of an active shield pushes and flexes the underlying lithosphere downward with upward flexing occurring some radial distance away from the load (Fig. 1). This process generates the Hawaiian moat and flexural arch surrounding the island chain, as are evident in bathymetric and gravity studies near Hawaii (e.g. *Watts et al.*, 1985, *Wessel*, 1993) and is seen in studies at other locations in the Pacific (*McNutt and Menard*, 1978). Clague and Dalrymple (1987) noted that the distance (or time) gap between shield volcanism and rejuvenation volcanism is similar to the distance (or time) gap between loading islands and the flexural arch. One of the strengths of this model is that it predicts both on- and off-shore secondary volcanism, however, this mechanism was not explored quantitatively. It is this mechanism that this work develops.

A successful model of secondary volcanism should predict the four key observations outlined above and summarized as: (1) a gap in space between the shield stage and secondary volcanism, (2) small volumes of secondary volcanism compared to the shield stage, and broad eruption areas in the case of arch lavas, (3) a proper isotopic distinction between secondary lavas and shield lavas, (4) a proper major element distinction between secondary and the tholeiitic shield lavas. This thesis proposes that the growth of an active shield volcano causes the rise of a flexural arch and asthenospheric decompression in an annular band around the shield (Fig. 1). I will show that the predicted spatial gap between the active shield and secondary volcanism is consistent with observations of

Hawaiian volcanism, and that volumes predicted are consistent with available constraints from the onshore events on Honolulu and the Hawaiian North Arch Lava Field. Further, I will show that differences in the pattern of mantle decompression beneath the arch and beneath the shield can account for differences in isotope and major element geochemistry.

2. Spatial and Temporal Correlations with Active Shields

In this section, I test whether flexure can explain the separation in distance between an active shield and secondary volcanism. The flexural model predicts rejuvenation to occur at some distance from an active shield. Figure 2 shows the time and distance of shield and secondary events relative to the active hotspot center. I measure the distances from the approximate center of rejuvenation to the approximate center of mass of any shield that was contemporaneously loading. For a single secondary volcanic event, there often are multiple, concurrently active shield loads. For example, during the time of rejuvenation volcanism on East Molokai, three shields also were active: Mauna Loa, Mauna Kea, and Kohala (Fig. 2). As all of these shields could be contributing to flexural uplift on East Molokai, I plot the distance between East Molokai and each of the three shields (Fig. 4A). The same measurements are repeated for all of the other rejuvenation events. To be conservative, I lengthen the time span of shield building beyond that inferred from dated lavas samples to reflect recent indications that the duration of the shield stage may be as long as 1.4 myr (e.g. *Guillou et al.*, 1997). However, I do not extend the time span of the shield stage of Kilauea Volcano because it is still relatively young (e.g. *DePaolo and Stolper*, 1996; *Quane et al.*, 2000). The data indicates what others have also recognized: that rejuvenation may contemporaneously occur over a large distance (e.g. *Taylor et al.*, 2004). However, while discrepancies exist, there is an increase in the frequency of secondary volcanic series correlated with particular radial distance from an active load. The results show that rejuvenation occurs between 150-600 km, but most frequently occurs ~200-400 km downstream from a loading island (Figure

4B). Arch volcanism occurs at slightly greater radial distances from loading shields (mostly 300-500 km).

To test whether these distances occur on the flexural arch, this work examines the axisymmetric flexural response due to a (volcano) point load. The problem requires solving for the rate of deflection of an elastic plate due to a single, linearly (in time) growing, transversal load (*Nadai*, 1931). Combining the constitutive law for bending of a thin elastic plate with the momentum equation, we obtain

$$\nabla^4 w + \frac{\Delta \rho g}{D} w = 0 , \tag{1}$$

at all (non-zero) radial distances from the point load. In (1), w is vertical displacement, $\Delta \rho$ is the density contrast between the crust and the mantle, g is gravitational acceleration, and D is flexural rigidity, and the operator ∇^4 is in radial coordinates and fully described in Appendix B (Eq. B2). Taking the time derivative of Nadai's solution of (1) provides the rate of flexure due to a growing point load. The solution is

$$\dot{w} = \frac{\dot{Q}}{4\sqrt{\Delta \rho g D}} \left[Re J_o(r') - Im Y_o(r') \right], \tag{2}$$

where $\dot{w}$ is the vertical displacement rate and, $\dot{Q}$ is the rate of growing force exerted by the concentrated point load on the plate, and *Re J₀* and *Im Y₀* are the real part of a (zeroth-order) Bessel function of the first kind and the imaginary part of a (zeroth-order) Bessel function of the second kind, respectively. The variable *r'* is radial distance normalized by the flexural parameter α,

$$r' = \frac{r\sqrt{j}}{\alpha} . \tag{3}$$

7

where r is radial distance and $j = \sqrt{-1}$. The distance to the flexural arch depends on the

effective elastic plate thickness T_e of the lithosphere through the relation between α and

the flexural rigidity D as follows (*Nadai*, 1931):

$$\alpha = \left(\frac{D}{\Delta \rho g} \right)^{1/4} \tag{4}$$

and

$$D = \frac{ET_e^{3}}{12\left(1 - \eta^{2}\right)}. \tag{5}$$

where E is Young's modulus and η is Poisson's ratio.

Figure 4C shows predicted flexure profiles for $T_e = 25$ and $T_e = 35$ km. The effective

elastic plate thickness controls the location and width of the flexural arch uplift. This

range of T_e is consistent with other estimates of the elastic plate thickness near Hawaii

(*Watts et al.*, 1985, *Wessel*, 1993) and predicts flexural uplift at distances from the

loading shield that overlap substantially with the distance of most frequent secondary

volcanism. While some secondary volcanism may have occurred outside of the predicted

region, the results indicate that the location of the majority of the secondary events are

consistent with the flexure model for $T_e = 25$ to 35 km.

3. Melting Model

3.1 Conceptual Model Description

In this section, I explore the fluxes and compositions of volcanism that flexural arch decompression can generate. Before describing the melting model in detail, I first provide a conceptual overview of the processes to be simulated. The model assumes the plume material is hot, and lithologically and chemically heterogeneous (e.g., *Frey and Rhodes*, 1993; *Hauri et al.*, 1996*; Lassiter et al.*, 1996). The hot material in the mantle plume stem upwells and melts at the hotspot center to create shield volcanism (Fig. 5). It is assumed that the melting stops as the material is diverted sideways by the base of the rigid lithosphere, and the residue of the melt flows horizontally (downstream from the hotspot and away from the axis of the island chain) in a layer beneath the lithosphere and forms a layer beneath the arch. If the lateral flow is rapid, this material has lost little heat due to conduction. Consequently, this layer is everywhere at its solidus, and any further decompression can cause secondary melting. The building of a new shield volcano at the hotspot center triggers this additional decompression under the flexural arch both along the island chain (onshore rejuvenated volcanism) and well away from the chain (e.g. the North and South Arch). The rate of asthenospheric upwelling beneath the rising arch varies predictably as a function of depth, and determines the flux of magma. Furthermore, the pattern of mantle upwelling beneath the flexing arch is distinct from that beneath the hotspot center. This difference influences the rate and extent of partial melting of the different mantle components and thus the isotope and major element geochemical distinctions between secondary and shield volcanism.

9

3.2 Mantle Flow Driven by Plate Flexure

The volume and composition of magma generated by arch decompression depends on the rate of asthenospheric upwelling as a function of depth below the lithosphere. I model the asthenosphere as an axisymmetric, fluid half-space. The fluid is isoviscous and incompressible, and is bounded above by a thin elastic layer (the lithosphere). The model assumes vertical velocity is continuous at the lithosphere/asthenosphere boundary, and therefore the base of the elastic layer uplifts at the same rate as the top of the fluid half-space. Also, there is a no-slip boundary condition assumed at this interface, and all velocities are zero at infinite depth. In the fluid layer, with zero acceleration, the invariant form of the Navier-Stokes equation describes momentum balance

$$\vec{\nabla}p - \rho\vec{B} = \mu\nabla^2\vec{v} \, . \tag{6}$$

(see also Table 1 for definition of variables). Here p is pressure as in Lai *et al.* (1999), ρ is the density of the asthenosphere, $\vec{B}$ is a body force (i.e., due to gravity), μ is viscosity, and $\vec{v}$ is the velocity vector. Since the model is axisymmetric, the gradient operator $\vec{\nabla}$ and the Laplacian operator ∇^2 are best described in cylindrical coordinates (see Appendix A). The model also assumes the asthenosphere is incompressible, thus the continuity equation takes the invariant form of

$$\vec{\nabla} \bullet \vec{v} = 0 \, . \tag{7}$$

(see Appendix A). Equations 6 and 7 represent three equations with three unknowns: the radial velocity v_r, the vertical velocity v_z, and the pressure p. The set of equations are subject to boundary conditions on the model. Specifically and most importantly, the

10

boundary condition at the surface of the half space is Eq. (2). The second and third boundary conditions specifies no vertical or radial velocity at infinite depth,

$$v_z(r, z \to \infty) = v_r(r, z \to \infty) = 0.$$ (8)

The fourth boundary condition specify no radial velocity at the surface,

$$v_r(r, z = 0) = 0.$$ (9)

Equations 6 through 9 may be solved analytically using Hankel transforms. Details of this calculation are in Appendix A and B. Appendix A outlines the formulation of the velocity problem in the asthenosphere and closely follows Sneddon (1951; pp. 307-310). Appendix B is the formulation and solution of (1) in Hankel space, so that rate of flexure in the lithosphere may be applied as a boundary condition on the asthenospheric half-space. Upwelling below the lithosphere boundary ($z > 0$) is given by (A21). A numerical evaluation using the trapezoid rule of (A21) produces an approximate solution for upwelling as a function of radial distance and depth

$$v_z(r, z) = \frac{\dot{Q}}{2\pi \Delta \rho g} \left\{ \sum_{\xi=0}^{\xi_{max}-\Delta\xi} \left[\frac{\xi^2 z + \xi}{(\alpha\xi)^4 + 1} \right] e^{-\xi z} J_0(\xi r) + \sum_{\xi=\Delta\xi}^{\xi_{max}} \left[\frac{\xi^2 z + \xi}{(\alpha\xi)^4 + 1} \right] e^{-\xi z} J_0(\xi r) \right\} \frac{\Delta\xi}{2}.$$ (10)

Here ξ is the transform parameter describing the "wavelength" of radial variations in v_z (analogous to wavenumber in a Fourier transform), $\Delta\xi$ is the interval of ξ used in the summation, ξ_{max} is the upper limit of the summation, and values necessary for acceptable convergence are listed in Table 1.

This thesis confirms this solution by using an independent method involving Fourier transforms. I take the 2-D Fourier transform of the Nadai solution in Cartesian coordinates. Incompressible flow beneath this surface boundary condition (*Turcotte and Schubert*, 2002; p. 239, Eq. 6-92) in Fourier space is

11

$$V_z(k,z) = \mathcal{F}\left\{\frac{\dot{Q}}{4\sqrt{\Delta\rho g D}}\left[\mathrm{Re}\,J_o(r') - \mathrm{Im}\,Y_o(r')\right]e^{-\kappa z}(1+\kappa)\right\}. \qquad (11)$$

Here V_z is the 2-D Fourier transform of v_z and κ is the magnitude of the wavenumber

vector, and $\mathcal{F}$ is the Fourier transform operator. An inverse Fourier transform of (11)

produces and independent check on v_z from (10). This method agrees with the Hankel

method to within a maximum error of $<10^{-4}$ of the peak vertical velocity at $z = 0$.

An example solution for v_z is shown in figure 6 (i.e., where upwelling is >0.1 of the

maximum). The flexing lithosphere is driving the flow of the asthenosphere and

therefore the most rapid flow is at the surface of the asthenosphere. Upwelling decays

(exponentially, Eq. 10, 11) with depth below the base of the lithosphere, but still remains

~40% of the lithosphere velocity at 70 km below the lithosphere, which is likely to

encompass most of the melting zone.

3.3 Melting Beneath the Flexural Arch

The above velocity solution determines the rate of asthenospheric decompression. To

compute the volume and composition of melts generated by decompression the model

must define how the extent of partial melting, F, varies as a function of depth in the

plume layer for each source component in the mantle.

Although previous work suggests the Hawaiian plume is a mixture of at least three

mantle source components (e.g. *Chen and Frey*, 1985), I simplify the model and

minimize the number of free parameters by considering the plume layer to be a mixture

of only two source components. The depleted component (DC) is assumed to be

anhydrous peridotite that is depleted in Sr and Nd relative to primitive mantle (*Sun and*

12

McDonough, 1989), has a low $^{87}Sr/^{86}Sr$ and a high $^{143}Nd/^{144}Nd$ isotope ratio (see Table 2 for values assumed), and an empirical solidus (*Hirschmann*, 2000). The second, enriched component (EC), has a high $^{87}Sr/^{86}Sr$ and a low $^{143}Nd/^{144}Nd$ isotope ratio. In one case, EC or EC1 is assumed to be hydrous peridotite. Because of the elevated water content, at the same temperature, EC1 will begin melting deeper than DC (e.g., *Katz et al*, 2003). In the second case, we assume EC or EC2 is pyroxenite, and it is enriched in Sr and Nd relative to primitive mantle. Like hydrous peridotite, pyroxenite will likely begin melting deeper in the mantle than the DC (*Pertermann and Hirschmann*, 2003). Both the isotopic ratio and the Sr and Nd contents of these materials are given values representative of the general characteristics of these materials. Figure 7A shows the solidus depth function for the three different materials, an example mantle adiabat, T_a, and an example temperature profile, T, assumed to be present in the plume layer beneath the arch.

Melt productivity, $\partial F/\partial p$, and F are calculated using basic principles of phase equilibria and thermodynamics (*Hirschmann et al.*, 1999, *Ito and Mahoney*, submitted, 2004*a*). The model assumes that the whole system is in thermal equilibrium, but the two components are chemically separate during melting (*Phipps Morgan*, 2001). Melt productivity is important because it determines the rate of melting,

$$\frac{\partial F}{\partial t} = \frac{\partial F}{\partial p}\frac{\partial p}{\partial t},$$ (12)

where the rate of pressure change, $\partial p/\partial t$, is proportional to mantle upwelling rate $v_z(r,z)$ since $p = \beta z$ where $\beta = 3.3\cdot10^{-2}$ GPa/km.

Figure 7B shows an example calculation of the productivity functions for a plume layer fed by a mantle plume stem that started (i.e., prior to melting at the hotspot center)

13

with a mean potential temperature of $\overline{T}_P = 1550\ ^{\circ}\text{C}$ (which is arbitrarily selected as an example $\overline{T}_P$). The productivity function is present beneath the arch because this material is the residue of melting at the hotspot center. The results show that arch decompression will cause EC1 (hydrous peridotite) to melt (i.e. $\partial F^{EC}/\partial p > 0$) throughout the plume layer. The productivity gradually increases with increasing extent of melting until dropping when clinopyroxene (cpx) is exhausted at $F = 0.2$. The melt productivity function for DC is qualitatively similar to that of EC1, but shifted to shallower depths. In this particular case, flexural decompression will cause DC melting to begin about halfway into the plume layer, and the plume layer is truncated by the base of the lithosphere before DC completes cpx exhaustion. Pyroxenite, (EC2) melting is predicted to start near the bottom of the plume layer, and both $\partial F/\partial p$ and F are predicted to increase rapidly until EC2 is consumed (i.e., $F = 1$), in this case, at ~ 20 km below the base of the lithosphere.

The amount each component contributes to the volume and geochemistry of the total secondary magma is determined by the integrated melt flux of the component in the starting mantle mixture under the arch

$$\dot{M}^i_{arch}(r) = \int_{z_1}^{z_2} \phi^i v(r,z') \frac{\partial F^i(z)}{\partial z} dz , \qquad (13)$$

where $\dot{M}^i_{arch}$ is the melt flux from component i (either DC or EC), ϕ^i is the mass fraction of the component, z_2 is the depth at the base of the lithosphere, z_1 is the depth at the base of the plume layer (Fig. 5), and $z' = z - z_2$ is the depth beneath the lithosphere. There are two important parameters that control (13), z_2 and $\overline{T}_P$. Altering z_2 affects the upwelling

14

function $v_z(r, z')$, while altering $\bar{T}_P$ affects the productivity function $\dfrac{\partial F^i(z)}{\partial z}$. For

example, a thicker lithosphere moves the lithosphere/asthenosphere boundary to greater

depth, and therefore the upwelling function $v_z(r, z')$ shifts uniformly to a greater depth,

while a higher plume potential temperature will move the productivity function to a

greater depth. Figure 8B illustrates an example calculation of how the incremental melt

flux (the integrand of Eq. 13) varies as a function of depth for a lithospheric thickness of

$z_2 = 90$ km and a mantle mixture of DC ($\phi^{DC} = 0.9$) and EC1 ($\phi^{EC1} = 0.1$). In this

example, the zone of greatest $\dfrac{\partial F^{DC}}{\partial z}$ (Fig. 7B) and the zone of greatest upwelling (Fig.

8A) are both near $z' = 90$ km, whereas the zone of greatest $\dfrac{\partial F^{EC1}}{\partial z}$ is ~15 km deeper

where upwelling is slower (Fig. 8A). These differences and the difference in mass

fraction ϕ^i lead to the greater area under the DC curve than under the EC1 curve.

The total integrated DC and EC1 fluxes, (13), for this same example are plotted on

Figure 9A, along with results using different values of z_2. Here it is seen that DC has a

higher flux than EC1 for lithospheric thickness between 50 and 115 km. Thus, for these

lithospheric thicknesses, DC melts are predicted to dominate the total volume and

composition of crust formed due to melting beneath the flexural arch.

3.4 Melting at the Hotspot Center

In this section, the melt flux under the flexural arch is contrasted with that predicted

beneath the hotspot center. Following Ito and Mahoney (submitted, 2004*a*), I compute

15

the melt flux for the entire hotspot melting zone by considering the extent of depletion, $F(z)$, and the radial flow rate $v_r(z)$ of all of the residue leaving the melt zone. The radial velocity $v_r(z)$ can be simply described by the flow profile in an expanding gravity current. The solution is

$$v_r(z') \propto (z_1 - z_2)z' - z'^2 ,$$ (14)

(*Huppert*, 1982) where in this case, $v_r(z')$ is the radial velocity at the edge of the melting zone, and therefore is not a function of r. The radial flow rate $v_r(z')$ determines the rate at which residue that melted by a fraction $F(z')$ exits the melting zone. The total melt flux of the melting zone from component i beneath the shield is thus the integral of the product of $v_r(z')$ and $F(z)$,

$$\dot{M}^i_{shield}(r) = \int_{z_1}^{z_2} \phi^i v_r(z') F^i dz .$$ (15)

As before, this manuscript provides an example calculation of the incremental melt flux as a function of depth (i.e., the integrand of Eq. 15) in Fig. 8C. The results for this scenario show that, compared to melting beneath the arch, the melting beneath the shield generates a larger flux of EC1. The main reason is that the quadratic increase in $v_r(z')$ with z' causes an increasing melt flux toward the base of the melting zone, where EC1 is dominantly melting. Figure 9 shows the effect of changing lithospheric thickness on total melt flux, $\dot{M}^i_{shield}$. In this example, for $z_2 > 80$ km, EC1 will dominate the contribution to the total crustal volume and geochemistry calculated for shield magmas.

3.5 Efficiency of Crustal Production by Flexural Arch Decompression

In order to compute the thickness of crust formed at the arch, the melt mass flux is converted to melt volume flux using the following equation:

$$\dot{h}_{cr}^i(r) = \frac{\rho_o}{\rho_L} \dot{M}_{arch}^i .$$

(16)

Here $\dot{h}_{cr}^i(r)$ is the volume flux of crust formed at a radius r, ρ_o is the density of the solid mantle, and ρ_L is the density of melted mantle (i.e., solid crust). I evaluate (13) and (16) for all radial distances over which arch uplift rate is positive, r_+. The maximum rate of crustal formation occurs at the radius of maximum rate of uplift. The average crustal production rate per meter of maximum uplift is

$$\dot{\bar{H}}_{cr} = \frac{\sum_{i}^{n} \int_{r_+} \dot{h}_{cr}^i dr}{r_+ w_{max}} ,$$

(17)

where $n = 2$, and w_{max} is the maximum uplift beneath the arch. We use results from (17) in subsequent calculations to compare predicted and observed rates of secondary volcanic crustal formation.

4. Magma Compositions

To solve for the Nd- and Sr-isotopic composition of magmas produced at the hotspot and beneath the flexing arch, I first compute the concentrations of these elements. The concentration of Nd and Sr in the melt is proportional to an enrichment function, which in this model assumes batch (or equilibrium) melting (e.g., *Albarède*, 1995),

$$E^i(z) = \left[F^i(z) + k_D (1 - F^i(z)) \right]^1. \tag{18}$$

Here $E^i(z)$ is the concentration of Nd or Sr in the incremental melt normalized by the starting concentration in the solid C_o^i (see Table 2) for component i, and k_D is the bulk distribution coefficient for the particular element. The average concentration of the element in the melt, C_L^i, is the average of the product of $E^i(z)$ and C_o^i weighted by the melt flux at each depth (*Albarède*, 1995)

$$C_L^i = C_o^i \left[\frac{\int_{z_1}^{z_2} E^i(z) \frac{\partial \dot{M}^i}{\partial z} dz}{\dot{M}^i} \right], \tag{19}$$

where $\dot{M}^i$ is the integrated flux for the appropriate melting zone and $\dfrac{\partial \dot{M}^i}{\partial z}$ is the integrand of (13) or (15). The total isotopic ratio in the final mixture, I^τ, is the weighted average

$$I^\tau = \frac{\sum_i^n I_o^i C_L^i \dot{M}^i}{\sum_i^n C_L^i \dot{M}^i}, \tag{20}$$

18

where I_o^i is the mean isotopic ratio in component i (see Table 2). We emphasize that these equations apply to melting of the residue of melting at the hotspot center; incompatible elements are still present in and extracted from depths near the DC and EC melting zones.

Finally, I calculate mean extent of partial melting, which is relevant to the major element properties of the melt. The appropriate calculation is F_v as discussed by Plank *et al.* (1995). For a single component,

$$F_v^i = \left[\frac{\displaystyle\int_{z_1}^{z_2} F^i(z) \frac{\partial \dot{M}^i}{\partial z} dz}{\dot{M}^i} \right]. \tag{21}$$

The total F_v is the weighted average of the contributions from each component,

$$F_v = f^i \left[\frac{\displaystyle\sum_i^n F_v^i \dot{M}^i}{\displaystyle\sum_i^n \dot{M}^i} \right]. \tag{22}$$

This work has adopted a factor f^i, which is designed to account for the different major-element compositions of peridotite and pyroxenite (*Ito and Mahoney*, 2004*a*). For the DC and EC1 components, $f^i = 1$, since they are both peridotite. For the EC2 component, this work assumes, $f^{PX} = 0.15$; with this assumption, 100% melting of the EC2 source will yield melts of the same composition as peridotites that melt to a mean fraction of 0.15.

5. Results

5.1 Efficiency of Crustal Production due to Flexural Arch Decompression

Many parameters control the amount and composition of crust in this model of flexural decompression. For simplicity, I report results with respect to three critical parameters: the relative fraction of each component in the mantle ϕ^i, the depth to the base of the lithosphere (i.e., lithospheric thickness) z_2, and the plume temperature $\overline{T}_P$.

Results are shown for three example sources arbitrarily chosen, but with the assumption that the plume will be predominantly DC. Case 1 is an EC1-DC plume where $\phi^{EC1} = 0.1$ and $\phi^{DC} = 0.9$. Case 2 is an EC2-DC plume where $\phi^{EC2} = 0.1$ and $\phi^{DC} = 0.9$. Case 3 is also an EC2-DC plume, but is mostly DC, $\phi^{EC2} = 0.001$ and $\phi^{DC} = 0.999$.

Figure 10 shows the predicted rate of crustal formation per meter of maximum uplift (i.e. the efficiency of crustal production), $\dot{\overline{H}}_{cr}$, from (17) for the three different component scenarios over a range of lithospheric thickness z_2 and mean plume potential temperature $\overline{T}_P$. All plume scenarios have the same general trend. For cooler plumes and thick lithosphere, crustal production efficiency is low. This occurs because at low $\overline{T}_P$ and large z_2, melting is restricted to a zone near or below the solidus of DC, and near the solidus of EC. Near the solidi, $\partial F^i / \partial z$ are low, and so is crustal production (see Eq. 13). Increasing $\overline{T}_P$ and decreasing z_2 results in larger rates of crustal formation as the height of the melting zone and $\partial F^i / \partial z$ increase. But at a certain limit, at high $\overline{T}_P$ and low z_2, $\dot{\overline{H}}_{cr}$ begins to decline because $\partial F^i / \partial z$ are again low. At these conditions the

peridotite (DC and EC1) have experienced cpx exhaustion and pyroxenite (EC2) is consumed.

This work now compares the rate of crustal formation of the different source scenarios for a single reference plume temperature of $\overline{T}_P$ = 1550 $^{\circ}$C. In Case 1, the most efficient rate of crustal production of 0.09 m/m$_{uplift}$ occurs for z_2 = 60 km. For Case 2, the most efficient melting is 0.11 m/m$_{uplift}$ with slightly thicker lithosphere, z_2 = 70 km. In Case 3, the most efficient melting of 0.09 m/m$_{uplift}$ occurs for z_2 = 58 km. Thus, the efficiency of melting tends to increase with the amount of pyroxenite in the mantle.

5.2 Difference in Isotope Compositions between Secondary and Shield Lavas

In order to compare predicted and observed isotopic differences between the shield (hotspot center) and secondary (arch) lavas, I use a normalized isotope difference ΔI,

$$\Delta I \ = \frac{I^{\tau}_{arch} - I^{\tau}_{shield}}{I^{EC}_o - I^{DC}_o} . \tag{23}$$

where I^{DC}_o is the assumed mean ratio in DC, and I^{EC}_o is the assumed mean ratio in EC. The observed ΔI is computed by taking the difference between the mean rejuvenation isotopic ratio and the mean shield ratio and normalizing this difference by $I^{EC}_o - I^{DC}_o$. The standard deviation of the observed ΔI is the sum of the standard deviation for the rejuvenation and shield lavas, normalized by $I^{arch}_o - I^{shield}_o$. The observed values (using data from the *GEOROC* database) are thus ΔI^{Nd} = 35% $\pm$ 15% and ΔI^{Sr} = 39.5% $\pm$ 12.5%. I normalize the computed variation by the difference in assumed component compositions in order to relate results to total possible variation.

21

Figure 11 shows theoretical values of ΔI. In all of these results, I observe a diagonal band (in $\overline{T}_P$-z_2 space) of maximum variation similar in shape and position to the region of maximum rate of crustal production ($\dot{\overline{H}}_{cr}$, Fig 10). I also see bands of low ΔI that are analogous to the low crustal productivity regions. The region of low ΔI at high z_2 and low $\overline{T}_P$ occurs because very little DC is melting and isotope compositions are restricted to be similar to that of the EC. The region of low ΔI at low z_2 and high $\overline{T}_P$ occurs because DC is dominating the melt flux and thus isotope compositions remain near that of DC. Within a band of high ΔI there are two bands in which the predicted isotope differences between secondary and shield volcanism matches to within one standard deviation of the observed mean differences. These thicknesses and temperatures allow for predominant melting of EC at the plume stem, and predominantly melting of DC at the flexural arch.

Other calculations (not shown) indicate that increasing ϕ^{EC} relative to ϕ^{DC} has the effect of shifting the contours to higher temperatures or to thinner lithospheres. To achieve the same ΔI (with greater ϕ^{EC} and lower ϕ^{DC}) conditions must be such to counteract the lower ϕ^{DC} by enhancing DC melting relative to EC. For a single temperature, thinner lithospheres increase DC melting, while for a single lithospheric thickness, higher temperatures augment DC melting over the thickness of the plume layer.

This work now identifies the values of $\overline{T}_P$ and z_2 that can produce the observed values of ΔI^{Nd} and ΔI^{Sr} for our set of reference values of ϕ^i, I_0^i, and $\overline{T}_P = 1550\,^{\circ}\text{C}$.

The best source compositions will have a common range of $\overline{T}_P$ and z_2 that predict observed ΔI for both Nd- and Sr-isotope systems. In Case 1 (Fig. 11A , B) observed isotope differences for both Nd and Sr are met with 50 km $< z_2 <$ 70 km. In Case 2 (Fig. 11C, D), agreement between both isotope systems requires 92 km $< z_2 <$ 104 km. For Case 3 (Fig. 11E, F), no overlap occurs between isotope systems for any temperature, and therefore Case 3 fails to predict observed isotopic agreement.

5.3 Mean Extent of Melting

To address the major element differences between the secondary and shield lavas this work now examines the mean extent of melting predicted by arch decompression and by melting at the hotspot center. Figure 12 shows the calculated mean extent of melting for the two remaining plume source scenarios that can match observed values of both ΔI^{Nd} and ΔI^{Sr}. These plots compare the mean extent of melting at the arch and at the plume stem for the reference temperature of $\overline{T}_P$ = 1550 ^oC. In both Case 1 and Case 2 there exists a range in z_2 where $F_v^{shield} > F_v^{arch}$. For Case 2, $F_v^{shield} > F_v^{arch}$ for z_2 = 90 to 100 km, the same thickness range which yielded successful matches to the observed ΔI^{Nd} and ΔI^{Sr}. At z_2 = 92 km, F_v^{shield} - F_v^{arch} is ~2.5%; at z_2 = 104 km, F_v^{shield} - F_v^{arch} = ~0.7%. In Case 1, the mean extent of melting is typically higher at the arch than at the hotspot center, except for z_2 = 82 to 102 km where $F_v^{shield} > F_v^{arch}$. This range of z_2 does not coincide with the range where calculations of ΔI matched observations. Thus, if secondary lavas form by a lower mean extent of partial melting than the shield lavas, Case 1 is not viable. Case 2 is thus the remaining successful mantle component model.

23

For this case, this thesis finds that $F_v^{shield} > F_v^{arch}$ at lithospheric thicknesses in agreement with lithospheric thicknesses necessary for observed isotope variations for a wide range of temperatures ($\overline{T}_P$ = 1400 to 1700 $^{\circ}$C).

6. Discussion

This thesis has tested a flexure model with respect to four observations of secondary volcanism of the Hawaiian Islands. The first test shows that the flexure model can predict the appropriate temporal and spatial separation between the active shield and secondary volcanism. Melting by flexural arch decompression can also yield the appropriate difference in Sr- and Nd-isotopes and lead to lower mean extents of melting compared to melting beneath the shield. This manuscript now discusses the volume of melt produced, explores some further implications of the flexure model, and presents shortcomings that require further study.

6.1 Observed and Calculated Crustal Formation

The purpose of this section is to compare model predictions with available constraints on the crustal production of secondary volcanism. Walker (1990) estimated an average melt flux of ~20 km^3/M.y. for Honolulu volcanics. The most efficient crustal production rate for the successful source (Case 2 in which z_2 yielded ΔI's consistent with the observations and $F_v^{shield} > F_v^{arch}$) is 0.063 m/m$_{uplift}$. To estimate absolute crustal thickness the model needs constraints on arch uplift. Geophysical studies infer ~5 km of deflection beneath Oahu (*Watts et al.*, 1985, *Watts and ten Brink*, 1989), resulting in ~75 m of uplift as predicted by the calculation of lithospheric flexure (Eq. 2). This value, however, may be a lower bound because erosion and mass wasting has significantly reduced the original load of Oahu (*Smith and Wessel*, 1998). Indeed, geologic evidence suggests Lanai, Molokai and Oahu may have uplifted (as this work assumes, due to loading associated with volcanism on Hawaii) by ~100 m (*Stearns*, 1978; *Jones*, 1993;

25

Griggs and Jones, 1997). Using 100 m uplift and estimating that it occurs over one

million years, the calculation predicts an average crustal production rate of 6.3 m/m.y. In

order to generate the estimated volume flux of 20 km^3/m.y., secondary eruptions of

Honolulu would have to draw magma from the decompressing mantle below an area of

~3200 km^2 (approximately equivalent to a circular area of radius 32 km). This model

does not include a melt focusing component, but one may exist. For example, aligning

the maximum principal stress in the plate, volcanic loads can sample magma propagating

in dikes from regions much larger than the eruption area (*ten Brink and Brocher*, 1987,

Hieronymus and Bercovici, 1999, 2001, *Muller et al.*, 2001). More precise measurement

of the flux of onshore secondary volcanism would allow for better estimates of the area

from which such focusing occurs.

Crustal production at the North Arch volcanic field has been estimated by Clague *et

al.* (2002) as ~40-50 m thick based on bathymetric surveys that covered about one-third

of the North Arch field and submersible surveys of at least one pit crater (122 m deep).

Again, assuming a total flexural arch uplift of 100 m, the model (using the Case 2 mantle)

predicts an average crustal thickness of 6.3 m. This prediction is smaller than the range

estimated by Clague *et al.* (2002). Perhaps some magma focusing occurs from a broader

region in the mantle to thicken the crust of the North Arch field. Another way to explain

thicker lava at the North Arch than this model predicts is to increase the number of

contemporary loads. Coeval shield activity may increase deflection both at the island

chain and at the arch. A larger deflection of the arch would produce more melt. For

example, load groups such as West Maui, Lanai, and East and West Molokai, or the

volcanoes on Hawaii could combine to increase deflection at the North and South Arch.

Multiple load geometry is also a method to get offshore secondary volcanism over distances and areas larger than the predicted uplift for a single load (Fig. 1 and 4). I also note that Clague *et al.'s* (2002) constraints on the thickness of the North Arch lava fields are weighted towards a single pit crater, and not an expansive survey of the area. To test or further constrain this model, the model needs better constraints on offshore as well as onshore eruption volumes.

6.2 Isotopic Variation

This model employs a two-component mantle. The isotopic compositions assumed for the components are mean compositions; they are not end-members, as they do not encompass the data (Fig. 3). In fact, the enriched component composition I_o^{EC} is representative of an average isotopic value employed to describe the whole range of the shield lavas, which themselves may be a mixture of two separate isotopic end-members that are presumably distinct from the DC component. It should be clear in Fig. 3 that there exists a bend in the Nd-Sr correlation, rendering a simple two end-member (or two-component) model insufficient to explain the combined shield and secondary lava data. This was also the conclusion of other Hawaiian volcanism research (e.g. *Staudigel et al.*, 1984; *Chen and Frey*, 1985). Taking the enriched component as a mixture of two sub-components (e.g. one with ($^{87}Sr/^{86}Sr$, $^{143}Nd/^{144}Nd$) = (0.7083,0.5130) and another with ($^{87}Sr/^{86}Sr$, $^{143}Nd/^{144}Nd$) = (0.7046, 0.5125)) could allow for this bend. Other work also shows best results for isotope trends that have a bend in the data by assuming source models that have three components (*Ito and Mahoney*, submitted, 2004*a*; 2004*b*).

Osmium isotope data also suggests the need for three isotopic sources involved in the formation of shield and secondary lavas. In contrast to the simple Nd-Sr correlation observed among shield and rejuvenation volcanism there is no apparent correlation between ^{187}Os /^{188}Os and ^{87}Sr/^{86}Sr among rejuvenation lavas. This may suggest that the high ^{187}Os/^{188}Os and low ^{87}Sr/^{86}Sr ratios of rejuvenated lavas come from a (pyroxenite) lithospheric source rather than a deep mantle plume source (*Lassiter et al.*, 2000; *Yang et al.*, 2003). This interpretation implies that flexural arch decompression is not the only cause of secondary melt (since the flexure model only allows for melting in the plume layer beneath the lithosphere). Alternatively, if the high ^{187}Os /^{188}Os source is in the plume layer, it must be distinct from any source this work has modeled, and must not be sampled significantly by plume melting.

6.3 Mean Extent of Melting and Major Elements

This manuscript now discusses the implications for mean extent of melting on the major element composition of lavas. I have made a very simple attempt to address differences in major element compositions between shield and secondary volcanism by computing mean extent of melting. The precise values of F_v^{shield} and F_v^{arch} depend on the rather crude correction factor, f^i. I also cannot yet address how low F_v^{arch} must be to yield the appropriate compositions. Thus far, the model produces a difference in F_v between secondary and shield lavas in the rights sense (i.e., $F_v^{shield} > F_v^{arch}$). Future efforts are necessary to explicitly compute major element compositions as in other models (e.g., *Asimow et al.*, 2001), to test whether flexural decompression of a

heterogeneous mantle can indeed generate alkalic secondary lavas (*Macdonald and Katsura*, 1964).

6.4 Validity of the Physical Properties of the Mantle

This work predicts good agreement for isotopic data and mean extent of partial melting data, and predicts significant crust formation, all with lithospheric thicknesses of ~90-100 km for an average plume temperature of 1550 ^{o}C and a plume composition that is 10% pyroxenite. The above range of lithospheric thicknesses is consistent with that expected for 90-m.y.-old oceanic lithosphere, according to the plate-cooling model (e.g., *Turcotte and Schubert*, 2002) and is consistent with some seismic studies around Hawaii (*Woods et al.*, 1991; *Woods and Okal*, 1996). Lower temperatures would require a thinner lithosphere to explain the data, which would be in agreement with other seismic data (e.g., *Bock*, 1991; *Priestley and Tilmann*, 1999; *Li et al.*, 2000). Furthermore, the reference mean plume potential temperature of 1550 ^{o}C is similar to that constrained by geodynamic studies of swell formation and crustal production (e.g., *Ribe and Christensen*, 1999). The reference model thus explains, to varying degrees of success, all four of the conditions with reasonable values of lithospheric thickness and mean plume temperature.

A final parameter worth further discussion is plume layer thickness. In the calculations I have shown, the layer of hot plume material downstream of the lithosphere ($z_2 - z_1$) is assumed to be 100 km. This work does not examine in detail the effects of varying plume layer thickness, but I have evaluated some general effects. Thinner layers tend to reduce the amount of crust generated, while thicker layers increase crustal

29

production. Different layer thicknesses require different values of z_2 and $\overline{T}_P$ to explain

the isotope differences and apparent low F_v for secondary lava compared to shields. One

seismic study that has constrained the thickness of a plume has estimated a thickness of

the Iceland plume to ≤ 200 km (*Allen et al.*, 2002). Future seismological studies to

better constrain the thickness of the plume layer will be valuable in further constraining

or testing the flexure model.

7. Conclusions

Secondary volcanism at Hawaii is manifested in two forms: onshore rejuvenated eruptions and the Hawaiian Arch eruptions. This thesis proposes a model in which the melt for both of these types of volcanism is generated as a direct consequence of the flexural uplift, which surrounds new volcanic shields as they grow. This uplift causes decompression of the underlying heterogeneous mantle plume material, which first melted partially beneath the shield, but has since flowed laterally away from the shield. In support of this model, this work has shown that secondary volcanism frequently occurs at locations predicted for the rising flexural arch of active volcanic shields. The predicted magma volume fluxes are comparable to crustal production rates of onshore and offshore secondary volcanism, if magma focuses from broad areas in the mantle to individual eruptions sites. The model successfully predicts Nd and Sr isotope observations for a range of lithospheric thickness, plume temperatures, and source mass ratio with a mixture of a depleted peridotite source and an enriched pyroxenite source. The same parameters also predict mean extent of partial melting results that are consistent with alkalic magma generated beneath the arch and tholeiitic magma generated in the plume stem. The most important model parameters are lithospheric thickness and mean mantle temperature. The reference values of these two parameters are consistent with constraints from recent geophysical studies. The main strength of the model is that it is able to predict many of the first order features of secondary volcanism. More insight into the physical and chemical properties of secondary volcanism and the mantle require more extensive analyses and improved data sets.

Table 1. General Constants and Variables

Symbol	Meaning	Assumed Values	Units
$\vec{B}$	Body force		m/s^2
C_o^i	Initial concentration in component i relative to primitive mantle		
D	Flexural rigidity	$9.72 \cdot 10^{22} - 26.7 \cdot 10^{22}$	$N \cdot m$
E	Young's Modulus	$70^{\dagger}$	GPa
F	Degree of partial melting		%
$\mathscr{F}$	Fourier transform operator		
F_v	Mean degree of partial melting		%
g	Gravitational acceleration	$9.8^{\dagger}$	m/s^2
$\mathscr{H}$	Hankel transform operator		
$\dot{h}_{cr}^i$	Volume melt flux beneath the flexural arch		$\dfrac{\% \cdot m}{s}$
$\dot{\vec{H}}_{cr}$	Rate of crustal formation		%/s
I_o^i	Initial isotopic ratio of component i		
I^{τ}	Final isotopic ratio		
ΔI	Isotopic variation between arch and shield melting zones		%
Im	Imaginary part of expression		
j	$\sqrt{-1}$		
J_0	Bessel function of the first kind, order zero		
k_D	Bulk distribution coefficient		
$\dot{M}_{arch}$	Mass melt flux beneath the flexural arch		$\dfrac{\% \cdot m}{s}$
$\dot{M}_{shield}$	Mass melt flux beneath the shield		$\dfrac{\% \cdot m^2}{s}$
n	Number of components in mantle	2	
p	"Pressure"		Pa
$\overline{P}$	First-order Hankel transform of non-lithostatic pressure beneath the flexural arch		N
$\dot{Q}$	Rate of growing point load		N/s
r	Radial distance		m
R	First-order Hankel transform of radial velocity beneath the flexural arch		$m^{-1} \cdot s^{-1}$
r'	Normalized radial distance		
r_+	Radial distance range of positive uplift		m
t	Time		s
T_e	Effective elastic plate thickness	$25\text{-}35^{\ddagger,\,\S}$	km

Table 1. (Continued) General Constants and Variables

Symbol	Meaning	Assumed Values	Units
$\bar{T}_P$	Mean potential temperature	1400-1700	$^{\circ}$C
v_r	Radial velocity		m/s
T_a	Adiabatic temperature		$^{\circ}$C
$\vec{v}$	Velocity beneath the flexural arch		m/s
V_z	Fourier transform of vertical velocity beneath the flexural arch		m^3/s
v_z	Vertical velocity beneath the flexural arch		m/s
w	Lithospheric deflection		m
$\dot{w}$	Rate of lithospheric deflection		m/s
$\dot{W}$	Zeroth-order Hankel transform of rate of lithospheric deflection		m^3/s
Y_0	Bessel function of the second kind, order zero		
z	Depth		m
Z	Zeroth-order Hankel transform of vertical velocity beneath the flexural arch		m^3/s
z'	Depth below the base of the lithosphere		
z_1	Depth of the base of the plume		
z_2	Depth of the base of the lithosphere		
α	Flexural parameter	66.7-85.9	km
β	Depth to pressure proportionality constant	3.3×10^{-2}	GPa/km
η	Poisson's ratio	0.25	
κ	Normalized wavenumber magnitude		m^{-1}
μ	Viscosity		Pa$\cdot$s
ξ	Normalized Hankel transform parameter		m^{-1}
ξ_{max}	Summation limit of ξ (Eq. 10)	250	m^{-1}
$\Delta\xi$	Summation interval of ξ (Eq. 10)	0.001	m^{-1}
ρ	Density of asthenosphere		kg/m^3
ρ_{crust}, ρ_L	Density of crust, liquid mantle	2800[†]	kg/m^3
ρ_{mantle}, ρ_o	Density of solid mantle	3300[†]	kg/m^3
$\Delta\rho$	ρ_{mantle} - ρ_{crust}	500	kg/m^3
ϕ^i	Mass fraction of component i		%

[†]*Turcotte and Schubert*, 2002; [‡]*Watts et al.*, 1985; [§] *Wessel*, 1993

Table 2. Assumed Component Compositions and Constants

	Depleted Component (DC)	Enriched Component (EC)	
$^{143}Nd/^{144}Nd$	0.51311	0.51277	
$^{87}Sr/^{86}Sr$	0.70295	0.70410	
	Concentration in Anhydrous Peridotite [#]	Concentration in Enriched Peridotite (EC1) [#]	Concentration in Pyroxenite (EC2) [#]
Nd	0.80	0.63	5.30
Sr	0.70	0.90	4.50
	Peridotite k_D		Pyroxenite k_D
Nd	0.0264		0.1500
Sr	0.0105		0.0678
# Element concentrations are normalized by the primitive mantle estimates of *Sun and McDonough*, 1989.			
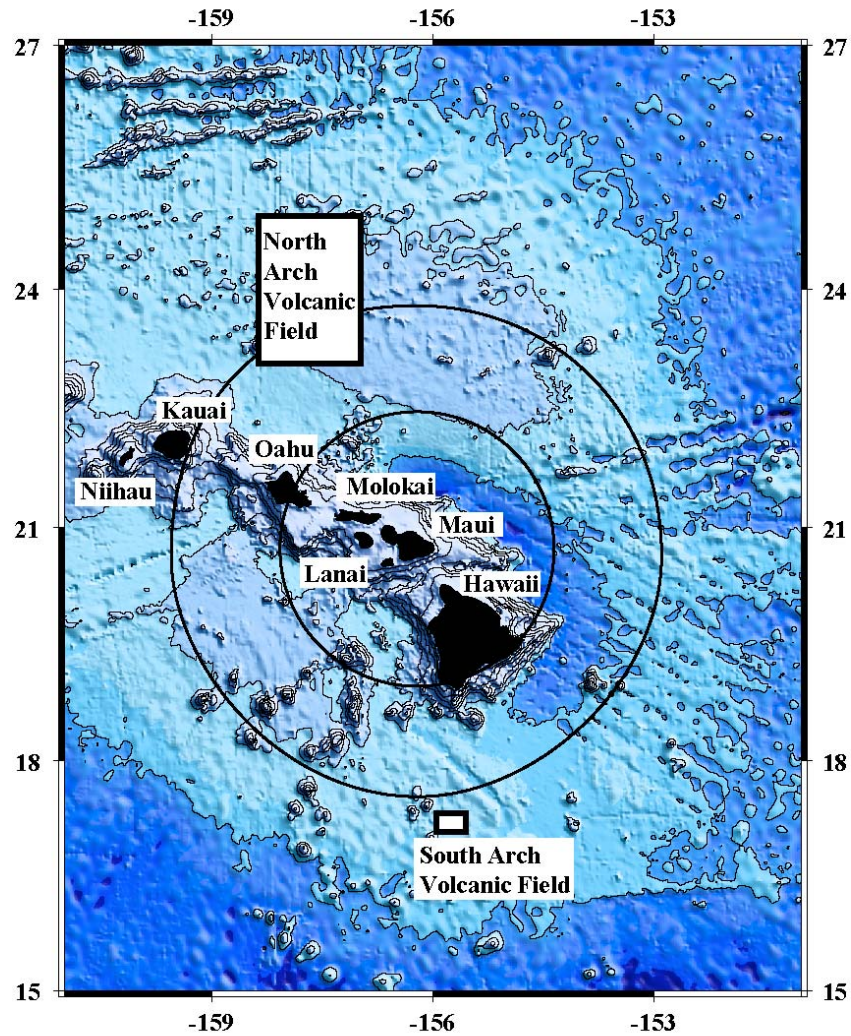
Figure 1. Map of the Hawaiian Islands and the surrounding Pacific Plate. Outlined boxes indicate approximate positions of the Hawaiian Arch Volcanic Fields, which straddle the raised bathymetry of the Hawaiian Arch. The inner black circle indicates the radius at which plate flexure due to a point load at the summit of Haleakala Volcano changes from downward deflection to upward deflection (assuming $T_e = 30$ km). The outer black circle encloses radii where positive deflection >10% of the maximum flexure.
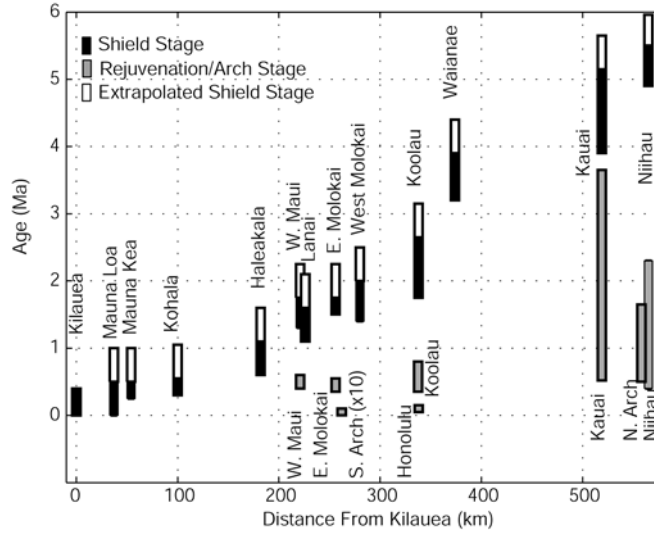
Figure 2. Modified from *Clague and Dalrymple*, 1987. Age and distance from Kilauea

Volcano (by including data from *Clague and Dalrymple*, 1988; *Lipman et al.*, 1989;

Clague et al., 2002; *Tagami et al.*, 2003; *Ozawa et al.*, 2004). Black bars represent shield

stage volcanism, gray bars represent secondary volcanism, and white bars represent

extrapolated shield stage (uniformly 500 ka to conservatively estimate duration of shield

volcanism, e.g., *Guillou et al.*, 1997). No extrapolation is added to the young Kilauea

Volcano (e.g. *DePaolo and Stolper*, 1996; *Quane et al.*, 2000). The time span of South

Arch volcanism is vertically exaggerated by ten times for visibility.
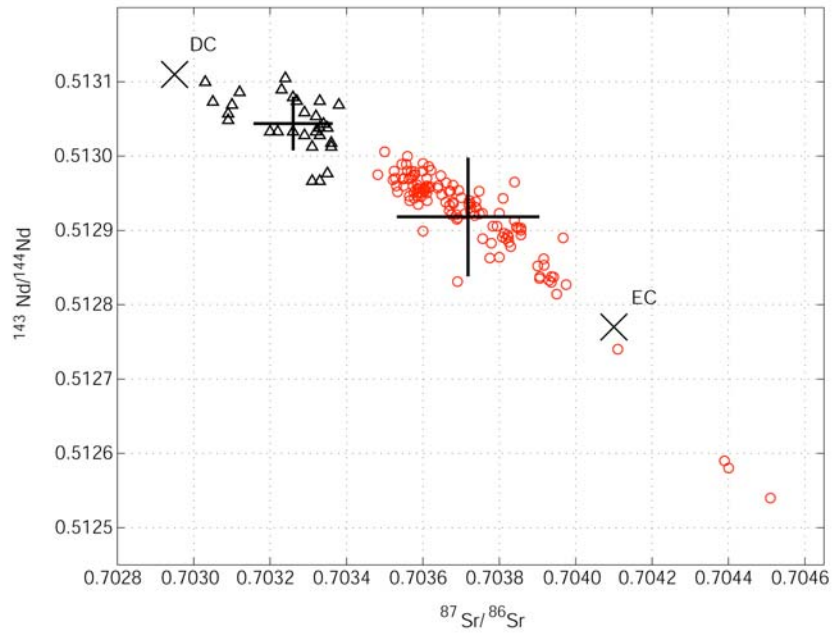
Figure 3. Isotope data. Hawaiian rejuvenation (triangles) and shield (circles) $^{143}Nd/^{144}Nd$ and $^{87}Sr/^{86}Sr$ isotope data (*GEOROC*). Average data and one standard deviation in both Nd and Sr isotope systems are marked with a black cross. Arbitrarily assumed mean compositions of DC (I_o^{DC}) and EC (I_o^{EC}) are shown by large X's.
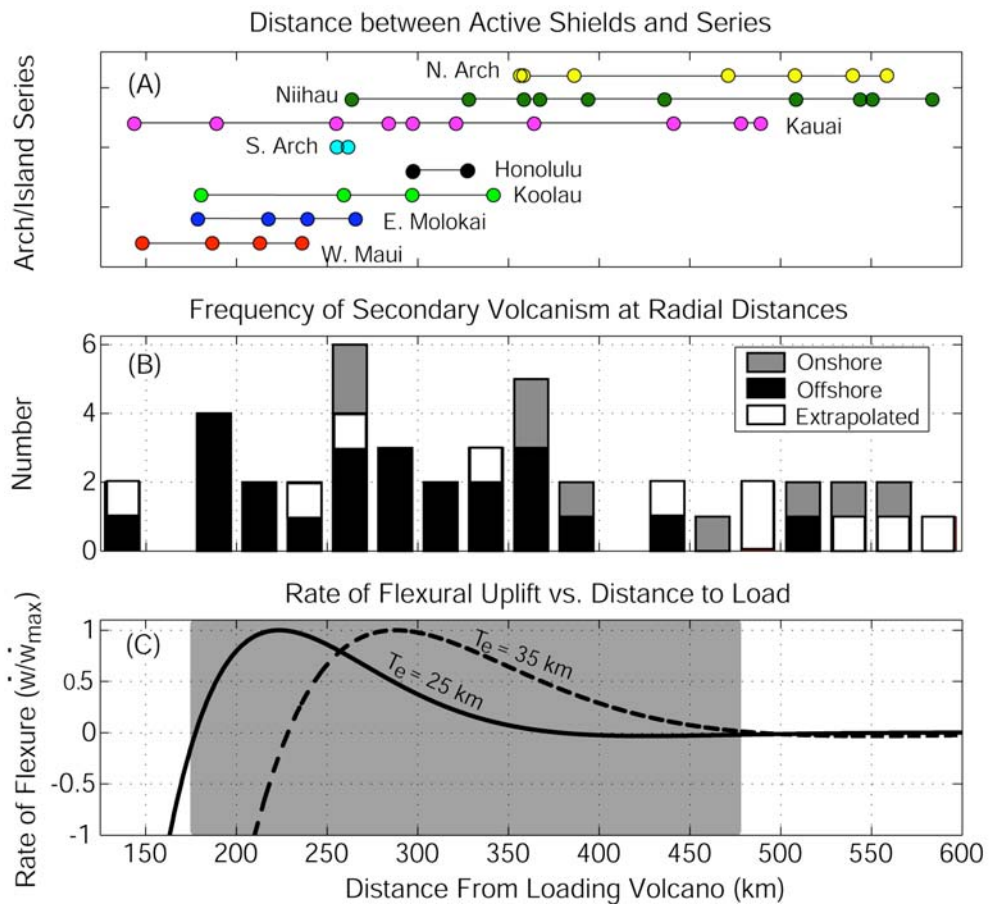
Figure 4. Spatial relation. (A) Circles show the distance between the labeled rejuvenation or arch series and contemporary active shield volcanoes. (B) A histogram of the population of shields active during secondary volcanism grouped by radial distance between the two types of volcanism. White bars are population data derived from the extrapolation of shield ages as in Fig. 2. (C). Normalized lithospheric rate of flexure profiles predicted (with Eq. 2) for effective elastic plate thickness of 25 km (solid) and 35 km (dashed). Gray shading shows the potential radial span of flexural uplift.
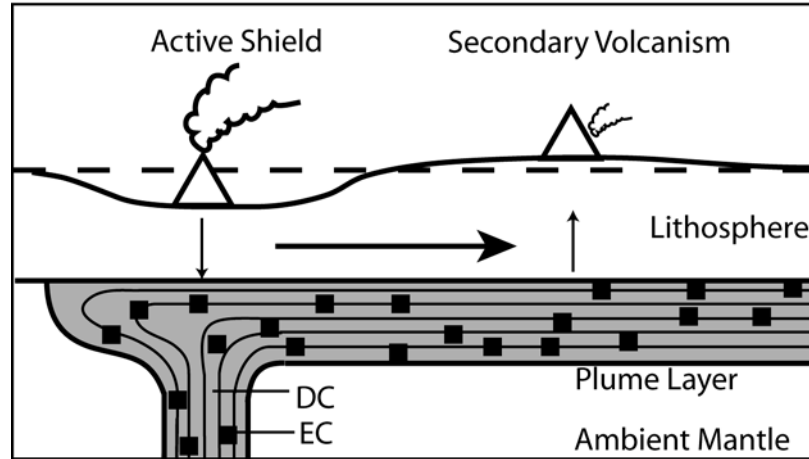
Figure 5. A schematic of the flexure model for secondary volcanism at Hawaii. Growth of the active shield pushes downward (downward pointing arrow) on the lithosphere beneath the shield and causes flexural uplift (upward pointing arrow) and secondary volcanism away from the shield. The curved line is an exaggerated example of how the lithosphere will flex compared to the unloaded lithosphere (dashed). The flexure also applies to the base of the lithosphere and top of the asthenosphere although here it is not shown. The large arrow shows the direction of plate motion which shears the plume layer below. The plume layer is on the order of thickness of the lithosphere and contains a depleted component matrix (DC) and an enriched component (squares; EC).
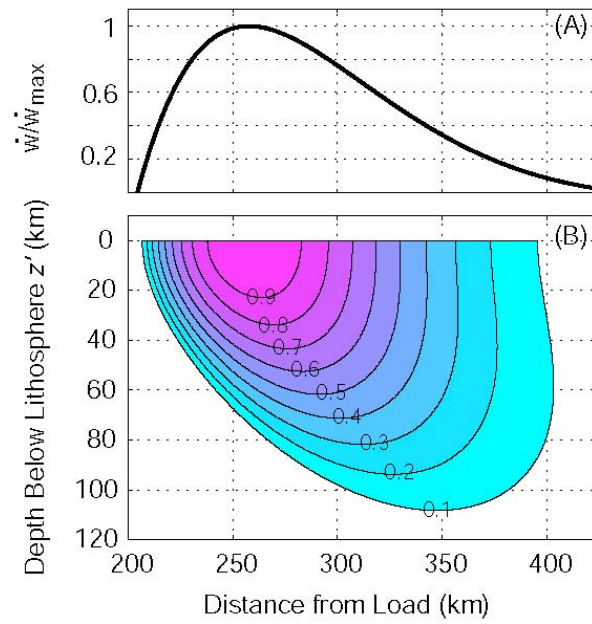
Figure 6. (A) Predicted rate of uplift of the flexural arch with elastic plate thickness T_e = 30 km. Curve is also the top surface boundary condition on the asthenosphere derived from (2). (B) Contours of upwelling rate beneath the flexural arch normalized by the peak uplift at the surface. The flow solutions are from (10).
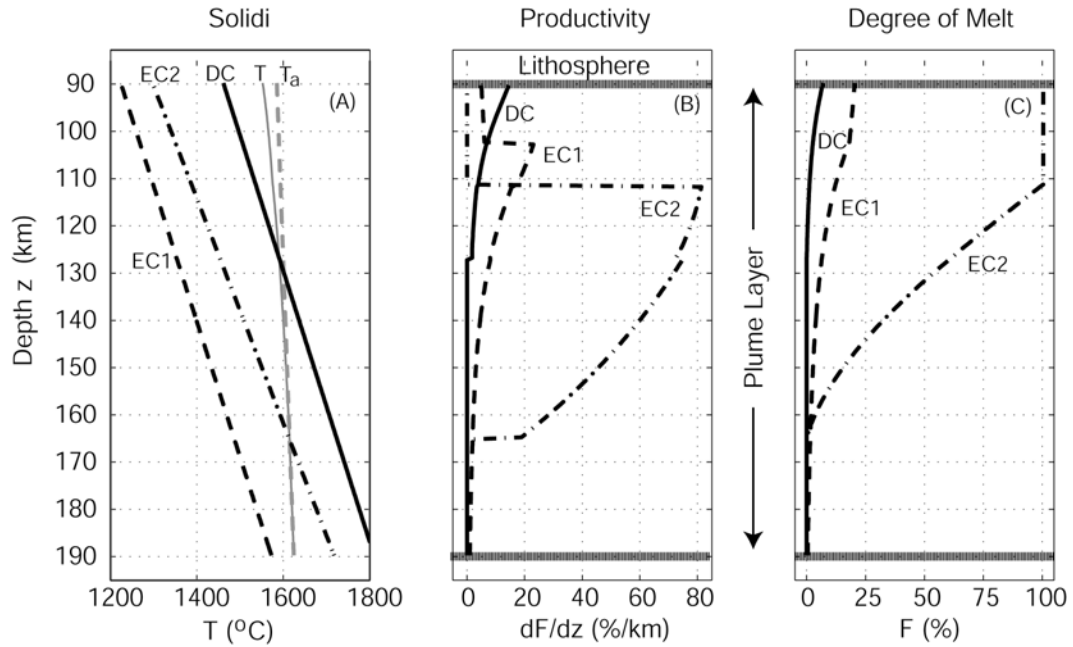
Figure 7. Melting functions. The above curves show the properties in the asthenosphere beneath the arch that remains after melting at the hotspot center. (A) Solidi of the enriched component as pyroxenite (*Pertermann and Hirschmann*, 2003; EC2, dash-dotted), the hydrous peridotite (EC1, dashed), and the depleted component as anhydrous peridotite (*Hirschmann*, 2000; DC, solid). The adiabatic temperature profile (T_a, dashed gray) is for a plume potential temperature of 1550 °C. The plume temperature profile (*T,* solid gray) varies from T_a due to latent heat loss in melting a mantle mixture of ~90% DC and 10% EC1 (some EC2 is added to allow for reasonable EC2 melting functions). (B) Melt productivities for each component (as labeled) vary greatly with depth. Here, I have also imposed a 90-km thick lithosphere and a 100 km-thick plume layer (i.e., melting can only occur between these depths). (C) The corresponding degree of melting as a function of depth. Curves in (B) and (C) are calculated using the method of Ito and Mahoney (submitted, 2004*a*).
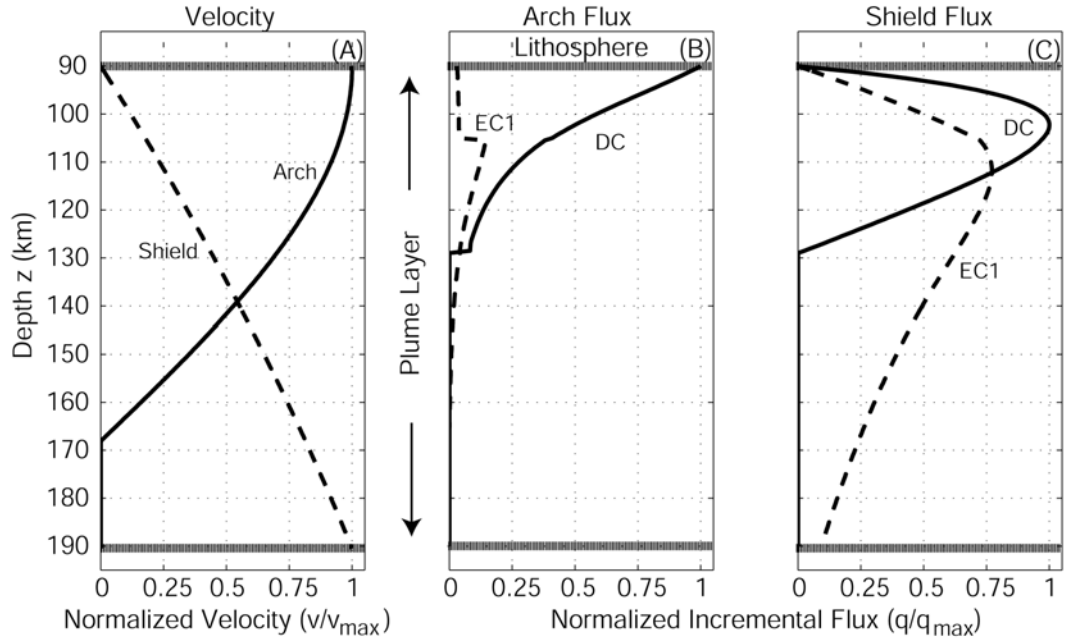
Figure 8. (A) Velocity profiles used to calculate melt flux for the flexural arch (solid, from Eq. 10) and the shield at the hotspot center (dashed, from Eq. 14). For the arch melting zone, the vertical velocity $v_z(r,z)$ profile is shown at the radius where the arch uplifts the fastest. Lithospheric thickness $z_2 = 90$ km, plume thickness is 100 km, and mean plume potential temperature is 1550 °C. (B) Incremental melt flux at the arch as a function of depth (the integrand of Eq. 13) normalized by the maximum integrand of the DC flux, for EC1 (dashed) and DC (solid) sources. In this example $\phi^{EC1} = 0.1$ and $\phi^{DC} = 0.9$. (C) Normalized incremental melt flux predicted for melting beneath the hotspot center (the integrand of Eq. 15) with the same source scenario as (B).
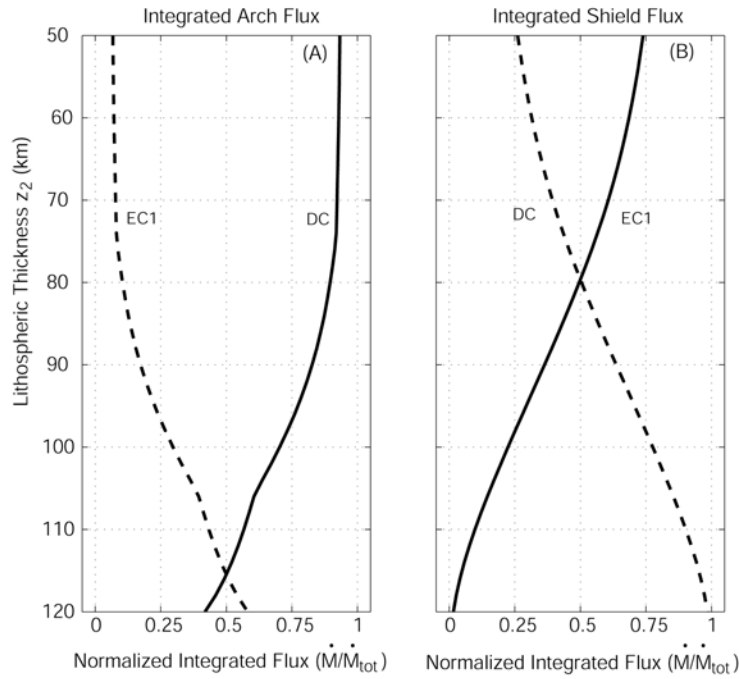
Figure 9. (A) Normalized integrated melt flux under the flexural arch for the plume

scenario as in Figure 8, for varying lithospheric thickness, z_2. EC1 (dashed) and DC

(solid) melt flux is integrated over the thickness of the 100 km thick plume layer. (B)

Normalized integrated melt flux calculated at the hotspot center. In both (A) and (B),

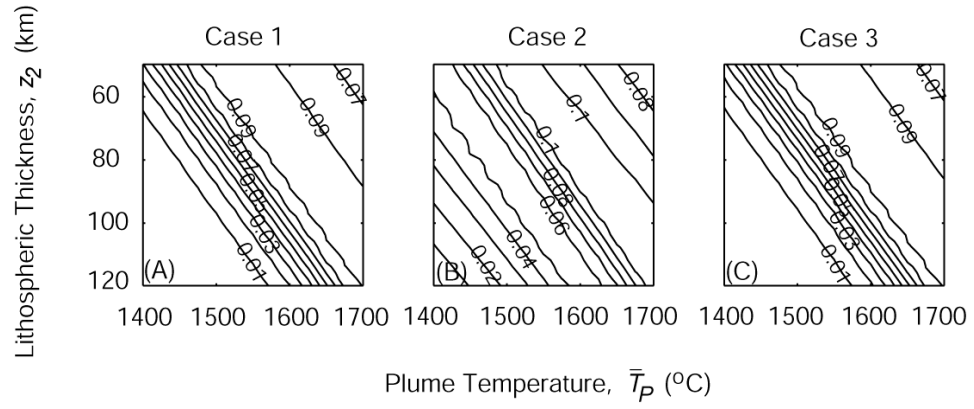$\phi^{EC1} = 0.1$ and $\phi^{DC} = 0.9$.

Figure 10. Efficiency of crustal production $\dot{\bar{H}}_{cr}$ (average thickness of magmatic crust per unit of maximum arch uplift; Eq. 17) formed from flexural decompression under the arch as a function of lithospheric thickness and plume temperature. (A) For Case 1: $\phi^{EC1} = 0.1$ (hydrous peridotite) and $\phi^{DC} = 0.9$ (anhydrous peridotite). (B) For Case 2: $\phi^{EC2} = 0.1$ (pyroxenite) and $\phi^{DC} = 0.9$. (C) For Case 3: $\phi^{EC2} = 0.001$ and $\phi^{DC} = 0.999$.
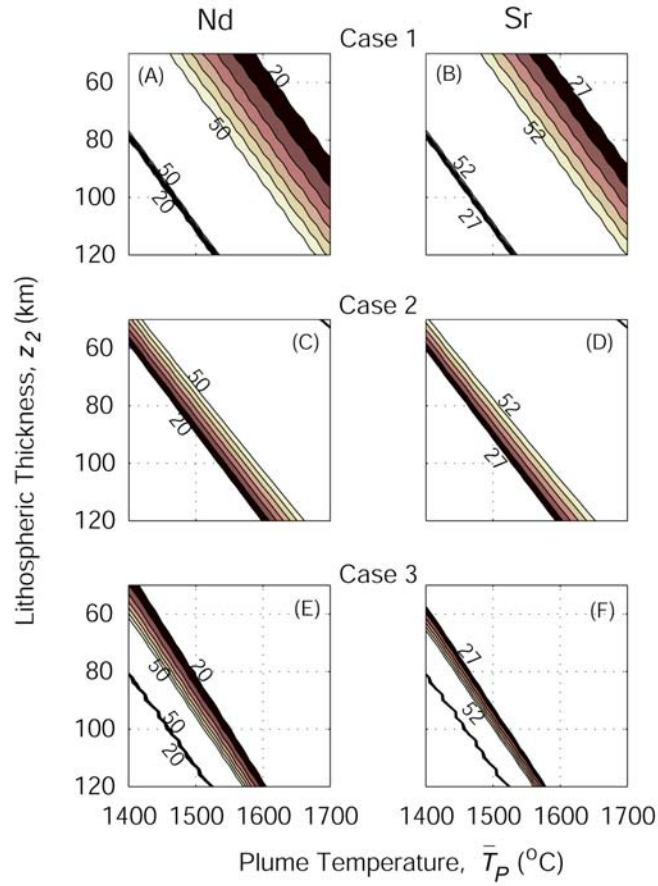
44

Figure 11. Predicted variation of normalized isotopic variation ΔI (Eq. 23) as a function of lithospheric thickness and plume temperature. Contours show values inside the observed range for Hawaiian lavas, at intervals of 0.05. White regions fall outside the observed range and are therefore rejected. (A), (C), (E) The ^{143}Nd/^{144}Nd variation for Case 1 ($\phi^{EC1} = 0.1$, $\phi^{DC} = 0.9$), Case 2 ($\phi^{EC2} = 0.1$ $\phi^{DC} = 0.9$), and Case 3($\phi^{EC2} = 0.001$, $\phi^{DC} = 0.999$), respectively. (B), (D), (F) The ^{87}Sr/^{86}Sr variation for Case 1, Case 2, and Case 3, respectively.
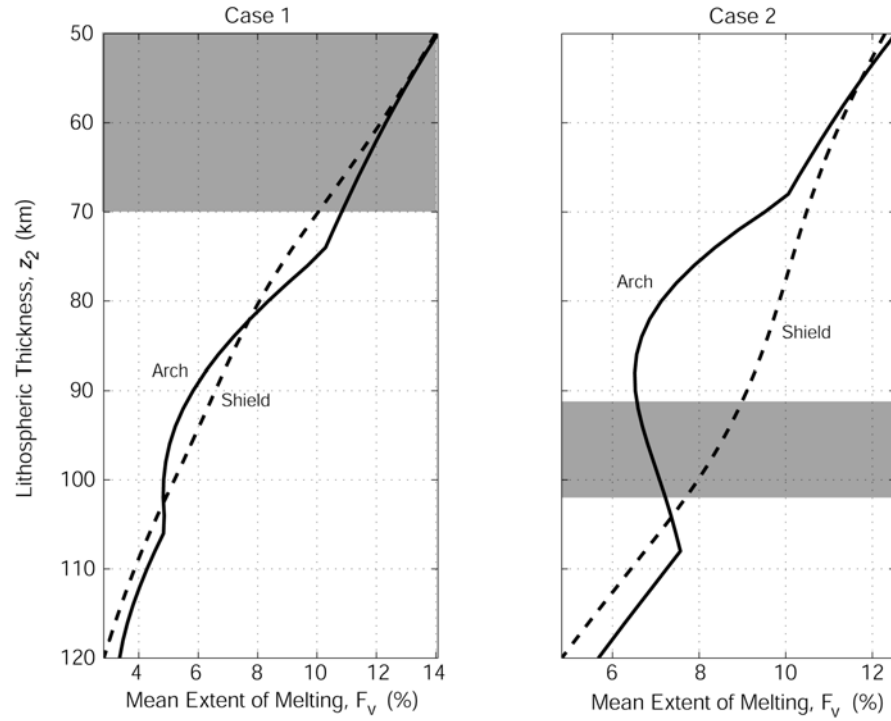
Figure 12. Mean extent of partial melting for $\overline{T}_P = 1550\ ^\circ\text{C}$ plume as a function of

lithospheric thickness (Eq. 22). (A) F_v in Case 1 where EC is EC1, hydrous peridotite

($\phi^{EC1} = 0.1$, $\phi^{DC} = 0.9$), for arch (solid) and shield (dashed) magmas. (B) As in Fig. (A)

for Case 2 where EC is EC2, pyroxenite ($\phi^{EC2} = 0.1$ $\phi^{DC} = 0.9$). The gray band marks

thickness values that have isotopic agreement for this scenario at the given plume

temperature (see Fig. 11A and B, C and D).

Appendix A. Solution for Flow of the Asthenosphere

Equations 6 and 7 govern flow of the asthenospheric model. In terms of non-lithostatic pressure $\bar{p}$

$$\bar{p} = p - \rho g z ,\qquad\qquad (A1)$$

(6) can be rewritten as momentum balance in the radial and vertical directions of a cylindrical coordinate system (and rotational terms are zero due to the assumption of axisymmetry). Radial momentum balance is described by (*Batchelor*, 1967; p. 602,)

$$\frac{1}{\mu}\frac{\partial \bar{p}}{\partial r} = \frac{1}{r}\frac{\partial}{\partial r}\left(r\frac{\partial v_r}{\partial r} \right) - \frac{v_r}{r^2} + \frac{\partial^2 v_r}{\partial z^2}\qquad\qquad (A2)$$

and vertical momentum balance is described page

$$\frac{1}{\mu}\frac{\partial \bar{p}}{\partial z} = \frac{1}{r}\frac{\partial}{\partial r}\left(r\frac{\partial v_z}{\partial r} \right) + \frac{\partial^2 v_z}{\partial z^2} .\qquad\qquad (A3)$$

Likewise, the continuity equation (Eq. 7) is

$$\frac{1}{r}\frac{\partial}{\partial r}\left(r v_r\right) + \frac{\partial v_z}{\partial z} = 0 .\qquad\qquad (A4)$$

The method of using transforms to simplify partial differential equations into ordinary differential equations is a common tactic. Here, the use of Hankel transforms is motivated by the problem's axisymmetry, and the fact that the surface boundary condition (Eq. 2) is described with Bessel functions.

As outlined in Sneddon (1951; pp. 307-310), I take the first-order Hankel transform of (A2). The first-order Hankel transform of the left hand side (LHS) of (A2) is thus

$$\mathcal{H}^1\left\{\frac{1}{\mu}\frac{\partial \bar{p}}{\partial z}\right\} = \frac{1}{\mu}\int_0^\infty \frac{\partial \bar{p}}{\partial r} r J_1(\xi r) dr .\qquad\qquad (A5)$$

Integration by parts yields

$$\mathcal{H}^1 \left\{ \frac{1}{\mu} \frac{\partial \overline{p}}{\partial z} \right\} = \frac{1}{\mu} \left[\overline{p} r J_1(\xi r) \Big|_0^\infty - \int_0^\infty \overline{p} [J_1(\xi r) + \xi r J_1'(\xi r)] dr \right]. \tag{A6}$$

where $\xi J_1'(\xi r) dr = \dfrac{\partial [J_1(\xi r)]}{\partial r}$. The first term of (A6) is zero, and using the recurrence

relation that

$$J_1'(x) = J_0(x) - \frac{1}{x} J_1, \tag{A7}$$

(*Abramowitz and Stegun*, 1970; p. 361, Eq. 9.1.27) the second term reduces to

$$\mathcal{H}^1 \left\{ \frac{1}{\mu} \frac{\partial \overline{p}}{\partial z} \right\} = \frac{-\xi}{\mu} \int_0^\infty \overline{p} r J_0(\xi r) dr, \tag{A8}$$

where the integral is the zeroth-order Hankel transform of $\overline{p}$, which this manuscript will

refer to as $\overline{P}$.

The first-order Hankel transform of the right hand side (RHS) of (A2) is

$$\mathcal{H}^1 \left\{ RHS(A2) \right\} = \int_0^\infty \frac{\partial}{\partial r} \left(r \frac{\partial v_r}{\partial r} \right) J_1(\xi r) dr - \int_0^\infty r \frac{v_r}{r^2} J_1(\xi r) dr + \int_0^\infty r \frac{\partial^2 v_r}{\partial z^2} J_1(\xi r) dr. \tag{A9}$$

The first integral is solved using integration by parts and Bessel's Equation to yield

$$\mathcal{H}^1 \left\{ RHS(A2) \right\} = \int_0^\infty \left[-\xi^2 r v_r J_1(\xi r) + \frac{v_r}{r} J_1(\xi r) \right] dr - \int_0^\infty \frac{v_r}{r} J_1(\xi r) dr + \int_0^\infty r \frac{\partial^2 v_r}{\partial z^2} J_1(\xi r) dr. \tag{A10}$$

The second term of (A10) conveniently cancels with the third. Also, this manuscript will

denote the first-order Hankel transform of v_r as R. Thus, combining (A8) with (A10)

yields the first-order Hankel transform of (A2)

$$-\frac{\xi}{\mu} \overline{P} = -\xi^2 R + \frac{\partial^2 R}{\partial z^2}. \tag{A11}$$

I take the zeroth-order Hankel transform of (A3) and (A4) which respectively yield

$$\frac{1}{\mu}\frac{\partial \overline{P}}{\partial z} = -\xi^2 Z + \frac{\partial^2 Z}{\partial z^2} \quad \text{and} \tag{A12}$$

$$\xi R + \frac{\partial Z}{\partial z} = 0, \tag{A13}$$

where Z is previously defined in the body of this thesis as the zeroth-order Hankel transform of vertical velocity, v_z.

Combining (A12) and the partial derivative of (A11) with respect to z and eliminates $\overline{P}$, yielding

$$\left(\frac{\partial^2}{\partial z^2} - \xi^2\right)Z + \frac{1}{\xi}\left(\frac{\partial^2}{\partial z^2} - \xi^2\right)\frac{\partial R}{\partial z} = 0. \tag{A14}$$

To eliminate R, I take the partial derivative of (A13) with respect to z and substitute the result in (A14) to produce the equation for the zeroth-order Hankel transform of vertical asthenospheric flow

$$\left(\frac{\partial^2}{\partial z^2} - \xi^2\right)Z - \frac{1}{\xi^2}\left(\frac{\partial^2}{\partial z^2} - \xi^2\right)\frac{\partial^2 Z}{\partial z^2} = 0. \tag{A15}$$

This result is more simply written as

$$\left(\frac{\partial^2}{\partial z^2} - \xi^2\right)^2 Z = 0. \tag{A16}$$

The general solution of (A16) is

$$Z = \left(A + Bz\right)e^{-\xi z} + \left(C + Dz\right)e^{\xi z}, \tag{A17}$$

where, A, B, C, and D are integration constants. Evaluation of (A13) gives

$$R = \left(A + Bz - \frac{B}{\xi}\right)e^{-\xi z} - \left(C + Dz - \frac{D}{\xi}\right)e^{\xi z} \tag{A18}$$

49

To resolve the four unknown constants, I apply the transformed boundary conditions.

The first boundary condition of $R(\xi, z \to \infty) = Z(\xi, z \to \infty) = 0$ requires that $C = D = 0$.

A second boundary condition for Z requires that it matches the rate of vertical motion of

the flexing lithosphere at $z = 0$. Thus,

$$Z(\xi, z = 0) = \frac{\dot{Q}}{2\pi\Delta\rho g}\left[\frac{1}{(\alpha\xi)^4 + 1}\right] = A \tag{A19}$$

(see Appendix B). To solve for the final unknown B, the boundary condition that

of $R(\xi, z = 0) = 0$ with respect to (A18) requires $B = \xi A$. Substitutions for A, B, C, and D

into (A17) yield,

$$Z(\xi, z) = \frac{\dot{Q}}{2\pi\Delta\rho g}\left[\frac{\xi z + 1}{(\alpha\xi)^4 + 1}\right]e^{-\xi z}. \tag{A20}$$

The inverse transformation of the upwelling velocity to spatial, cylindrical coordinates is

given by (also Eq. 10)

$$v_z(r, z) = \frac{\dot{Q}}{2\pi\Delta\rho g}\int_0^\infty Z(\xi r)J_0(\xi r)\xi d\xi . \tag{A21}$$

A numerical approximation to (A21) using the trapezoid rule is given in (10).

Appendix B. Hankel Transform of the Surface Boundary Condition: Eq. A19

In order to apply the rate of flexure as a boundary condition on the asthenosphere model, the solution must be expressed as a zeroth-order Hankel transform. Nadai's solution (Eq. 2) is not readily transformed, thus the original problem (i.e., Eq. 1) must be formulated and solved in Hankel space. In cylindrical coordinates, the first term of (1) is

$$\nabla^4 \dot{w} = \frac{1}{r} \frac{\partial}{\partial r} \left\{ r \frac{\partial}{\partial r} \left[\frac{1}{r} \frac{\partial}{\partial r} \left(r \frac{\partial \dot{w}}{\partial r} \right) \right] \right\}. \tag{B1}$$

The boundary conditions of this problem as given by Nadai (1931) are

$$\dot{w}(r \to \infty) = 0, \tag{B2}$$

$$\dot{w}(r = 0) = finite, \tag{B3}$$

$$\frac{\partial \dot{w}}{\partial r}(r = 0) = 0, \text{ and} \tag{B4}$$

$$\frac{\partial \nabla^2 \dot{w}}{\partial r} = \frac{\dot{Q}}{2\pi D r}. \tag{B5}$$

Taking the zeroth-order Hankel transform of (B1) and integrating by parts yields

$$\mathcal{H}^0 \left\{ \nabla^4 \dot{w} \right\} = r \frac{\partial \nabla^2 \dot{w}}{\partial r} J_0(\xi r) \bigg|_0^\infty - \xi \int_0^\infty \frac{\partial}{\partial r} \left[\frac{1}{r} \frac{\partial}{\partial r} \left(r \frac{\partial \dot{w}}{\partial r} \right) \right] r J_o'(\xi r) dr, \tag{B6}$$

where $\xi J_o'(\xi r) dr = \dfrac{\partial \lfloor J_0(\xi r) \rfloor}{\partial r}$. Applying (B5) reduces (B6) to

$$\mathcal{H}^0 \left\{ \nabla^4 \dot{w} \right\} = -\frac{\dot{Q}}{2\pi D} - \xi \int_0^\infty \frac{\partial}{\partial r} \left[\frac{1}{r} \frac{\partial}{\partial r} \left(r \frac{\partial \dot{w}}{\partial r} \right) \right] r J_0'(\xi r) dr. \tag{B7}$$

Further integration of the second term of (B7), while applying the remaining boundary conditions, reveals that the zeroth order Hankel transform of (B1) is

51

$$\mathcal{H}^0\left\{\nabla^4\dot{w}\right\} = -\frac{\dot{Q}}{2\pi D} + \xi^4\dot{W} , \tag{B7}$$

where $\dot{W}$ is the zeroth-order transform of $\dot{w}$. Combining this result with the zeroth-order transform of the second term in (1) yields the expression

$$\dot{W}(\xi) = \frac{\dot{Q}}{2\pi\Delta\rho g}\left[\frac{1}{(\alpha\xi)^4 + 1}\right] = Z(\xi, z = 0) \tag{B8}$$

To remind the reader, $Z(\xi, z = 0)$ is the first-order Hankel transform of asthenospheric vertical velocity at the lithosphere/asthenosphere boundary. This is the boundary condition given in (A19).

Literature Cited

Abramowitz, M., and I.A. Stegun, Handbook of Mathematical Functions, Dover Publications, Inc., New York, USA, 1970.

Albarède, F., *Introduction to Geochemical Modeling*, 543 pp., Cambridge University Press, Cambridge, 1995.

Allen, R.M., G. Nolet, W.J. Morgan, K. Vogfjord, B.H. Bergsson, P. Erlendsson, G.R. Foulger, S. Jakobsdottir, B.R. Julian, M. Pritchard, S. Rangarsson, and R. Stefansson, Imaging the mantle beneath Iceland using integrated seismological techniques., *J. Geophys. Res.*, *107* (B12), doi:10.1029/2001JB000595, 2002.

Asimow, P.D., M.M. Hirschmann, and E.M. Stolper, Calculation of peridotite partial melting from thermodynamic models of minerals and melt, IV. Adiabatic decompression and the composition and mean properties of mid-ocean ridge basalts, *J. Petrol.*, *42* (5), 963-998, 2001.

Batchelor, G.K., *An Introduction to Fluid Dynamics*, 615 pp., Cambridge University Press, Cambridge, UK, 1967.

Bock, G., Long-period S to P converted waves and the onset of partial melting beneath Oahu, Hawaii., *Geophys. Res. Lett.*, *18*, 869-872, 1991.

Chen, C.-Y., and F.A. Frey, Trace element and isotopic geochemistry of lavas from Haleakala Volcano, East Maui, Hawaii, *J. Geophys. Res.*, *90* (B10), 8743-8768, 1985.

Clague, D.A., and G.B. Dalrymple, The Hawaiian-Emperor Volcanic Chain, *U. S. Geol. Surv. Prof. Pap.* (1350), 5-54, 1987.

Clague, D.A., and G.B. Dalrymple, Age and petrology of alkalic postshield and rejuvenated stage lava from Kauai, Hawaii, *Contributions to Mineralogy and Petrology*, *99*, 202-218, 1988.

Clague, D.A., R.T. Holcomb, J.M. Sinton, R.S. Detrick, and M.E. Torresan, Pliocene and Pleistocene alkalic flood basalts on the seafloor north of the Hawaiian Islands, *Earth Planet. Sci. Lett.*, *98*, 175-191, 1990.

Clague, D.A., K. Uto, K. Satake, and A.S. Davis, Eruption style and flow emplacement in the submarine North Arch Volcanic Field, Hawaii, in *Hawaiian Volcanoes: Deep Underwater Perspective*, edited by E. Takahashi, P.W. Lipman, M.O. Garcia, J. Naka, and S. Aramaki, pp. 65-84, American Geophysical Union Monograph 128, 2002.

Crough, S.T., Thermal origin of mid-plate hotspot swells, *Geophys. J. Roy. Astr. Soc.*, *55*, 451-469, 1978.

Depaolo, D., and E.M. Stolper, Models of Hawaiian volcano growth and plume structure: Implications of results from the Hawaii Scientific Drilling Project, *J. Geophys. Res.*, *101* (B5), 11643-11654, 1996.

Detrick, R.S., and S.T. Crough, Island Subsidence, hot spots, and lithospheric thinning, *J. Geophys. Res.*, *83* (B3), 1236-1244, 1978.

Dixon, J.E., D.A. Clague, P. Wallace, and R. Poreda, Volatiles in alkalic basalts from the North Arch Volcanic Field, Hawaii, *J. Petrol.*, *38* (7), 911-939, 1997.

Frey, F.A., D.A. Clague, J.J. Mahoney, and J.M. Sinton, Volcanism at the edge of the Hawaiian plume, *J. Petrol.*, *44* (5), 667-691, 2001.

Frey, F.A., and J.M. Rhodes, Intershield geochemical differences among Hawaiian volcanoes, *Philosophical Transactions of the Royal Society of London*, *342*, 121-136, 1993.

Grigg, R.W., and A.T. Jones, Uplift caused by lithospheric flexure in the Hawaiian Archipelago as revealed by elevated coral deposits, *Mar. Geol.*, *141*, 11-25, 1997.

Guillou, H., M.O. Garcia, and L. Turpin, Unspiked K-Ar dating of young volcanic rocks from the Loihi and Pitcairn seamounts, *J. Volcanol. Geotherm. Res*, *78*, 239-249, 1997.

Gurriet, P., A thermal model for the origin of post-erosional alkalic lava, Hawaii, *Earth Planet. Sci. Lett.*, *82*, 153-158, 1987.

Hieronymus, C.F., and D. Bercovici, Discrete alternating hotspot islands formed by interaction of magma transport and lithospheric flexure, *Nature*, *397*, 604-607, 1999.

Hieronymus, C.F., and D. Bercovici, Focusing of eruptions by fracture wall erosion, *Geophys. Res. Lett.*, *28*, 1823-1826, 2001.

Hirschmann, M.M., Mantle Solidus: Experimental constraints and the effects of peridotite composition, *Geochem. Geophys. Geosyst.*, *1*, doi:2000GC000070, 2000.

Hirschmann, M.M., P.D. Asimow, M.S. Ghiorso, and E.M. Stolper, Calculation of peridotite partial melting from thermodynamic models of mineral melts. III. Controls on isobaric melt production and the effect of water on melt production, *J. Petrol.*, *40* (5), 831-851, 1999.

Huppert, H.E., The Propagation of two-dimensional and axisymmetric viscous gravity currents over a rigid horizontal surface, *J. Fluid Mech.*, *121*, 43-58, 1982.

Ito, G., and J.J. Mahoney, Flow and melting of a heterogeneous mantle: 1. Method and importance to the geochemistry of ocean island and mid-ocean ridge basalts, *Earth Planet. Sci. Lett.*, Submitted, 2004a.

Ito, G., and J.J. Mahoney, Flow and melting of a heterogeneous mantle: 2. Implications for a chemically non-layered mantle, *Earth Planet. Sci. Lett.*, Submitted, 2004b.

Jackson, E.D., and T.L. Wright, Xenoliths in the Honolulu Volcanic Series, *J. Petrol.*, *11*, 405-430, 1970.

Jones, A.T., Review of the chronology of marine terraces in the Hawaiian Archipelago, *Quaternary Science Review*, *12*, 811-823, 1993.

Katz, R.F., M. Spiegelman, and C.H. Langmuir, A new parameterization of hydrous mantle melting, *Geochem. Geophys. Geosyst.*, *4* (9), doi:10.1029/2002GC000433, 2003.

Lai, W.M., D. Rubin, and E. Krempl, *Introduction to Continuum Mechanics*, 3rd Edition. Butterworth-Heinemann, USA, 1999.

Lassiter, J.C., E.H. Hauri, P.W. Reiners, and M.O. Garcia, Generation of Hawaiian Post-Erosional Lavas by melting of a mixed lherzolite/pyroxenite source, *Earth Planet. Sci. Lett.*, *178*, 269-284, 2000.

Li, X., R. Kind, K. Priestley, S.V. Sobolev, F. Tilmann, X. Yuan, and M. Weber, Mapping the Hawaiian Plume with converted seismic waves, *Nature*, *405*, 938-941, 2000.

Lipman, P., Declining growth of Mauna Loa during the last 100,000 years: Rates of lava accumulation vs. gravitational subsidence, in *Mauna Loa Revealed: Structure,*

Composition, History, and Hazards, edited by J.M. Rhodes, and J.P. Lockwood, pp. 45-80, American Geophysical Union Monograph 92, 1995.

Lipman, P., D.A. Clague, J.G. Moore, and R.T. Holcomb, South Arch Volcanic Field-Newly identified young lava flows on the sea floor south of the Hawaiian Ridge, *Geology*, *17*, 611-614, 1989.

Lui, M., and C.G. Chase, Evolution of Hawaiian Basalts: A Hotspot melting model, *Earth Planet. Sci. Lett.*, *104*, 151-165, 1991.

Macdonald, G.A., and T. Katsura, Chemical composition of Hawaiian Lavas, *J. Petrol.*, *5*, 82-133, 1964.

McNutt, M., and W.H. Menard, Lithospheric flexure and uplifted atolls, *J. Geophys. Res.*, *83*, 1206-1212, 1978.

Moore, J.G., D.A. Clague, and W.R. Normark, Diverse basalt types from Loihi Seamount, Hawaii, *Geology*, *10*, 88-92, 1982.

Muller, J.R., G. Ito, and S.J. Martel, Effects of volcano loading on dike propagation in an elastic half space, *J. Geophys. Res.*, *106* (B6), 11,101-11,113, 2001.

Mysen, B.O., and I. Kushiro, Compositional variation of coexisting phases with degree of melting of peridotite in the upper mantle, *American Mineralogist*, *62*, 843-865, 1977.

Nadai, A., *Theory of Flow and Fracture of Solids*, 260-269 pp., McGraw-Hill Book Co., New York, 1931.

Ozawa, A., T. Tagami, and M. Garcia, Abstract: Magmatic pulses in the Honolulu rejuvenated-stage volcanism: evidence from K-Ar dating, in *Cities on Volcanoes 3*, Hilo, Hawaii, 2003.

Pertermann, M., and M.M. Hirschmann, Partial melting experiments on a MORB-like pyroxenite between 2 and 3 GPa: Constraints on the presence of pyroxenite in basalt source regions from solidus locations and melting rate., *J. Geophys. Res.*, *108* (B2), doi:10.1029/2000JB 000118, 2003.

Phipps Morgan, J., Thermodynamics of pressure release melting of a veined plum pudding mantle, *Geochem. Geophys. Geosyst.*, *2* (4), doi:2000GC000049, 2001.

Plank, T., M. Spiegelman, C.H. Langmuir, and D.W. Forsyth, The meaning of "mean F:" Clarifying the mean extent of melting at ocean ridges, *J. Geophys. Res.*, *100* (B8), 15,045-15,052, 1995.

Priestley, K., and F. Tilmann, Shear-wave structure of the lithosphere above the Hawaiian Hot Spot from two-station Rayleigh Wave phase velocity measurements, *Geophys. Res. Lett.*, *26*, 1493-1496, 1999.

Quane, S., M.O. Garcia, H. Guillou, and T. Hulsebosch, Magmatic history of Kilauea Volcano based on drill core from SOH1:Implications for the structure of the Hawaiian Plume, *Journal of Volcanology*, *102* (3-4), 319-338, 2000.

Ribe, N.M., and U.R. Christensen, The Dynamical origin of Hawaiian Volcanism, *Earth Planet. Sci. Lett.*, *171*, 517-531, 1999.

Roden, M.F., F.A. Frey, and D.A. Clague, Geochemistry of tholeiitic and alkalic lavas from the Koolau Range, Oahu, Hawaii: Implications for Hawaiian Volcanism, *Earth Planet. Sci. Lett.*, *62*, 215-228, 1984.

Smith, J.R., and P. Wessel, Isostatic consequences of giant landslides on the Hawaiian Ridge, *Pure and Applied Geophysics*, *157*, 1097-1114, 2000.

Sneddon, I.N., *Fourier Transforms*, 1st Edition. International Series in Pure and Applied Mathematics. 542 pp., McGraw-Hill Book Company, Inc., New York, USA, 1951.

Staudigel, H., S. Hart, A. Zindler, M. Lanphyre, C.-Y. Chen, and D.A. Clague, Pb, Nd, Sr isotopes of Loihi Seamount, Hawaii, *Earth Planet. Sci. Lett.*, *69*, 13-29, 1984.

Stearns, H.T., *Geology of the Hawaiian Islands*, 2nd Printing. Hawaiian Division of Hydrography Bulletin 8. 112 pp., 1967.

Stearns, H.T., Quaternary shorelines in the Hawaiian Islands, *Bishop Museum Bulletin*, *237*, 1-57, 1978.

Sun, S.-S., and W.F. McDonough, Chemical and isotopic systematics of oceanic basalts: Implications for mantle compositions and processes, in *Magmatism in the Ocean Basins*, edited by A.D. Saunders, and M.J. Norry, pp. 313-345, Geological Society of London Special Publication, 1989.

Tagami, T., Y. Nishimitsu, and D.R. Sherrod, Rejuvenated-stage volcanism after 0.6-m.y. quiescence at West Maui Volcano, Hawaii: New evidence from K-Ar ages and chemistry of Lahaina Volcanics, *J. Volcanol. Geotherm. Res*, *120* (3-4), 207-214, 2003.

Taylor, B., B. Applegate, G. Ito, M. Garcia, G.F. Moore, J. Smith, I. Van der Zander, R. Dunn, and J. Hammer, Submarine Volcanism Around Kauai, *Earth Planet. Sci. Lett.*, Submitted, 2004.

ten Brink, U.S., and T.M. Brocher, Multichannel seismic evidence for a subcrustal intrusive complex under Oahu and a model for Hawaiian Volcanism, *J. Geophys. Res.*, *92* (B13), 13,687-13,707, 1987.

Turcotte, D.L., and G. Schubert, *Geodynamics*, 2nd Edition. 456 pp., Cambridge University Press, Cambridge, 2002.

Walker, G.P.L., Geology and volcanology of the Hawaiian Islands, *Pacific Science*, *44* (4), 315-347, 1990.

Watts, A.B., U.S. ten Brink, P. Buhl, and T.M. Brocher, A multichannel seismic study of lithospheric flexure across the Hawaiian-Emperor Seamount Chain, *Nature*, *315*, 105-111, 1985.

Wessel, P., A reexamination of the flexural deformation beneath the Hawaiian Islands, *J. Geophys. Res.*, *98* (B7), 12,177-12,190, 1993.

Wilson, J.T., A Possible origin of the Hawaiian Islands, *Canadian Journal of Physics*, *41*, 863-870, 1963.

Yang, H.-J., F.A. Frey, and D.A. Clague, Constraint on the source components of lavas forming the Hawaiian North Arch and Honolulu Volcanics, *J. Petrol.*, *44* (4), 603-627, 2003.